metals

MDPI

Article

The Influence of the Ratio of Circumference to Cross-Sectional Area of Tensile Bars on the Fatigue Life of Additive Manufactured AISI 316L Steel

Luka Ferlič [1], Filip Jerenec [1], Mario Šercer [2], Igor Drstvenšek [1] and Nenad Gubeljak [1,*]

[1] Faculty of Mechanical Engineering, University of Maribor, 2000 Maribor, Slovenia; luka.ferlic@um.si or luka.ferlic@gmail.com (L.F.); filip.jerenec@um.si or filip.jerenec@gmail.com (F.J.)
[2] Metal Center Čakovec, Bana Jelačića 22D, 40000 Čakovec, Croatia; ravnatelj@metalskajezgra.hr
* Correspondence: nenad.gubeljak@um.si or nenadxgubeljak@gmail.com

Abstract: The static and dynamic loading capacities of components depend on the stress level to which the material is exposed. The fatigue behavior of materials manufactured using additive technology is accompanied by a pronounced scatter between the number of cycles at the same stress level, which is significantly greater than the scatter from a material with the same chemical composition, e.g., AISI 316L, but produced by rolling or forging. An important reason lies in the fact that fatigue cracks are initiated almost always below the material surface of the loaded specimen. Thus, in the article, assuming that a crack will always initiate below the surface, we analyzed the fatigue behavior of specimens with the same bearing cross section but with a different number of bearing rods. With a larger number of rods, the circumference around the supporting part of the rods was 1.73 times larger. Thus, experimental fatigue of specimens with different sizes showed that the dynamic loading capacity of components with a smaller number of bars is significantly greater and can be monitored by individual stress levels. Although there are no significant differences in loading capacity under static and low-cycle loading of materials manufactured with additive technologies, in high-cycle fatigue it has been shown that the ratio between the circumference and the loading cross section of tensile-loaded rods plays an important role in the lifetime. This finding is important for setting a strategy for manufacturing components with additive technologies. It shows that a better dynamic loading capacity can be obtained with a larger loading cross section.

Keywords: AISI 316L stainless steel; additive manufacturing; FEM; high-cycle fatigue; fractography analysis

Citation: Ferlič, L.; Jerenec, F.; Šercer, M.; Drstvenšek, I.; Gubeljak, N. The Influence of the Ratio of Circumference to Cross-Sectional Area of Tensile Bars on the Fatigue Life of Additive Manufactured AISI 316L Steel. *Metals* **2024**, *14*, 1246. https://doi.org/10.3390/met14111246

Academic Editor: Zhixin Zhan

Received: 20 September 2024
Revised: 21 October 2024
Accepted: 24 October 2024
Published: 2 November 2024

1. Introduction

Additive manufacturing (AM) presents numerous advantages over traditional manufacturing, enhancing cost-effectiveness and sustainability. It facilitates the production of complex geometries quickly, reducing both development time and waste [1]. AM's advanced capabilities also allow the creation of previously impossible designs, optimizing weight for critical applications in the aerospace [2,3], automotive [4–8], and medical fields, including implants [9,10] and prostheses [11,12].

AISI 316L stainless steel is particularly suitable for AM due to its high corrosion resistance. It is used widely in demanding sectors such as the nuclear, petrochemical, chemical, and food industries [13], benefiting from low thermal conductivity and a high melting point. Its stability in oxygen-rich environments and high absorptivity make it ideal for AM processes [14].

Several AM technologies are employed in manufacturing AISI 316L, including powder bed fusion (PBF), directed energy deposition (DED), fused deposition modeling (FDM), and binder jetting (BJ) [15]. PBF and DED are notable for producing near-full-density

components with mechanical properties close to those of traditionally manufactured materials [15]. Reports suggest that AM materials can even surpass the mechanical properties of their conventional counterparts [16].

Given the real-world applications of AM 316L parts, such as in the aerospace and automotive industries, these components are subject to cyclic loading, necessitating thorough fatigue characterization. Typically, untreated AM 316L parts show lower fatigue life compared to wrought counterparts, underscoring the influence of inherent AM challenges [14].

The additive manufacturing process for metals involves complex thermal management. The laser's movement and the localized melting pool leads to rapid solidification rates (106 K/s) [17], imposing a complex thermal history on the material. This process generates significant residual stresses, particularly tensile stresses on free surfaces [18], which affect both the mechanical and fatigue properties critically [19]. Predominantly, heat dissipates in the Z-direction toward the build platform, resulting in a columnar microstructure that contributes to the anisotropic material properties [17]. Although microstructural inhomogeneity impacts the material fatigue behavior significantly, surface and internal defects are predominant in high-cycle-fatigue scenarios, with microstructure anisotropy playing a secondary role [17,20].

Internal defects, dependent on process parameters [21], include porosity and lack of fusion pores (LOF) [22]. High power density can cause keyhole porosity, forming spherically shaped pores from trapped gases [23]. Gases encapsulated within powder particles can also be released during melting [24]. LOF pores, resulting from inadequate molten pool penetration, create non-welded areas with higher stress concentrations than gas porosity defects [25,26]. These LOF defects, due to their orientation and irregular shape, influence fatigue behavior critically, more so than smaller defects [27,28]. Microcracks, another defect type, form during solidification due to rapid cooling and contribute to further material degradation [29,30].

Insufficient energy input leads to the balling effect, where partially melted particles stick to build surfaces, increasing surface roughness significantly [31]. The inherent step-by-step layer building process increases this roughness [32]. However, surface roughness is not the only factor affecting part quality. All the previously mentioned internal defects can also manifest on or near surfaces, qualifying as surface defects [17]. These defects, comparable in size to internal defects but with higher stress concentration factors [21,33], impact the fatigue life of components significantly [17].

Extensive research shows that cracks typically initiate from critical surface locations [29,33,34]. For 316L stainless steel, fatigue behavior studies under various surface conditions have shown that specimens retaining their original surface roughness exhibit lower fatigue properties than machined counterparts, even when the AM parts achieve near-full density (99.3–99.7%) [27,35,36]. To enhance the fatigue properties, surface treatments such as polishing or machining are necessary, as they remove near-surface defects and reduce stress concentrations [27].

While surface treatments influence performance positively, the complex geometries of additive manufactured parts often make complete machining impractical. Additional machining increases both production time and costs, potentially offsetting the advantages of AM. Critical defects in AM components are typically located near surfaces. Estimating porosity using the Archimedes method is relatively straightforward [37], but this alone is insufficient for determining fatigue strength relative to defects. Predictive models, such as that of Murakami [38], require knowledge of the defect area, unobtainable through the Archimedes method. To assess defect distribution and size, optical microscopy, a destructive method, is employed alongside non-destructive X-ray computed tomography [37]. However, obtaining detailed defect information is both costly and time-consuming, challenging the benefits of additive manufacturing.

Many studies on the fatigue properties of AM components focus on standard fatigue specimens, typically featuring circular or rectangular cross sections. This standard geometry maintains a constant ratio between the outer surfaces and near-surface defects compared

to internal defects. However, additive manufacturing enables far more complex shapes, e.g., topologically optimized geometries that might not maintain a similar defect-to-load-bearing-area ratio. Consequently, this study aims to evaluate the impact of the ratio between the outer surface and cross-sectional area on the fatigue behavior of additive manufactured components made from AISI 316L steel.

2. Materials and Methods

Through numerical simulations, two structure specimen arrangement geometries were designated for fatigue testing. Each specimen type was designed with a constant cross-sectional area of 38.1 mm^2;. The configurations included a 4-rod specimen, with each rod having a diameter of 3.48 mm, and a 12-rod specimen where each rod's diameter was 2.01 mm. The diameter of the 12-rod specimen geometry was chosen to be at least 2 mm in respect to the maximum stress capacity. From experience, maximum stress is reduced with small diameters of specimens(d < 1 mm); therefore, minimizing the diameter was needed for comparable results. Choosing the diameter of 2.01 mm for the 12-rod geometry also allowed all the specimens to be manufactured at the same time, reducing the material property differences between specimens. Furthermore, 4- and 12-rod geometries were selected to obtain as high a ratio as possible of outer surface to cross-sectional area while keeping the geometries within the limitations of the test and manufacturing equipment. These specific dimensions resulted in distinct ratios of outer surface area to cross-sectional area: 0.44 for the 4-rod design and 0.25 for the 12-rod design, as shown in Table 1 and Figure 1. Additionally, tensile specimens intended for tensile testing were utilized to evaluate mechanical properties and are shown in Figure 1c. Due to the standardized nature of the tensile specimens, finite element analysis was deemed unnecessary for these specimens, and it was performed only for specimens with 4 and 12 rods.

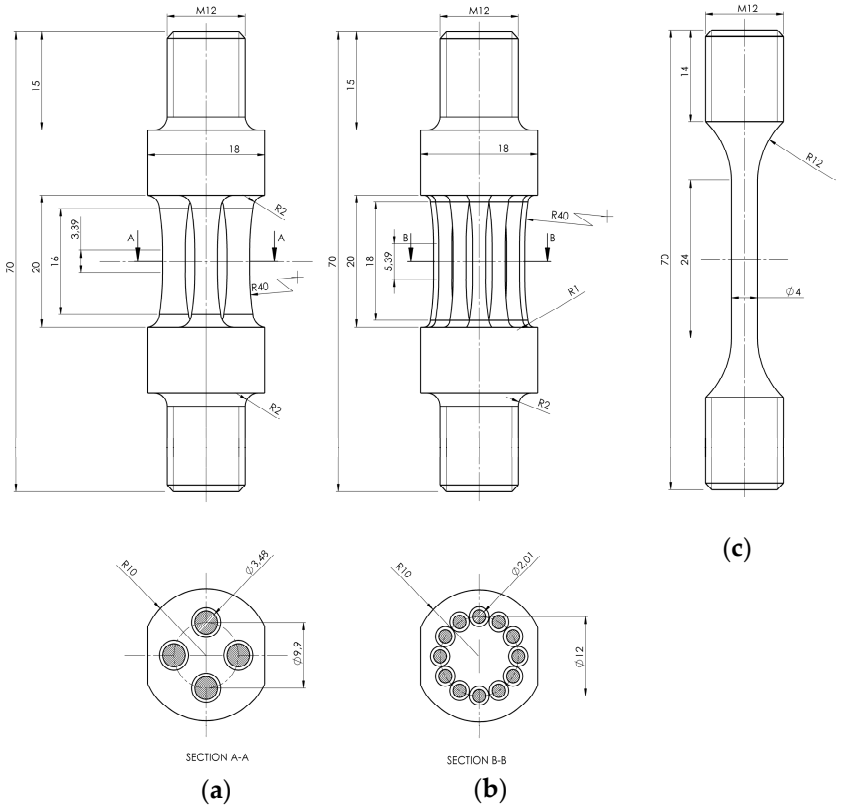

Figure 1. The geometry and dimensions of specimens with (**a**) 4 bars and (**b**) 12 bars and of (**c**) a tensile specimen. All dimensions in mm.

Table 1. Geometric configurations of N4 and N12 specimens.

Specimen Design	Number of Rods	Diameter (mm)	Area of Rod (mm^2)	Total Area (mm^2)	Total Circumference (mm)	Ratio Area/Circumference (mm)
N4	4	3.48	A_4 = 9.51	38.1	87.52	0.44
N12	12	2.01	A_{12} = 3.17	38.1	151.6	0.25

2.1. Finite Element Analysis of Geometries

Finite element analysis (FEA) was utilized to simulate stress distribution across these complex geometries and identify potential stress concentrations, particularly at points where the rod geometries transitioned to the threaded ends of the specimens. Ensuring effective cyclic loading, threading was integrated at each end of the specimens, where all loading rods converged onto a single thread. This setup necessitated meticulous design considerations to mitigate stress concentrations at these critical connection points. Stress relief was achieved by introducing transitional radii at the junctions, with the dimensions determined through an iterative process until stress concentrations were reduced to acceptable levels.

Moreover, the design process also addressed the specific challenges posed by additive manufacturing technologies, such as limitations regarding overhang surfaces without support. This was crucial in determining viable geometries that could be manufactured effectively without compromising the structural integrity or accuracy of the fatigue tests.

By leveraging the symmetry inherent in both designs, symmetry boundary conditions were applied, allowing for the modeling of only one-eighth of the actual geometry. This simplification is depicted clearly in Figures 2 and 3, which illustrate the symmetry and boundary conditions of the models with 4 bars and 12 bars, respectively. Further simplifications were made by excluding threading from the analysis.

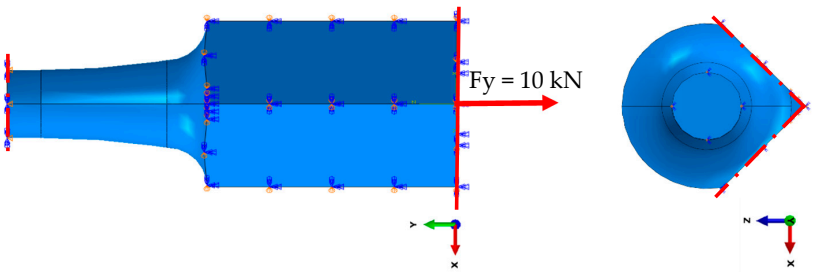

Figure 2. Numerical model and boundary conditions for the N4 geometry.

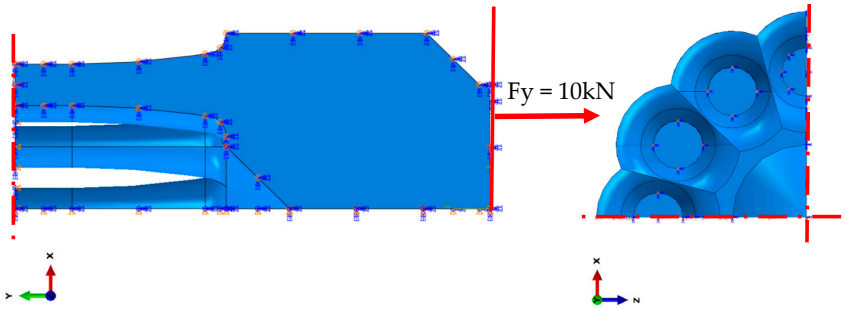

Figure 3. Numerical model and boundary conditions for the N12 geometry.

The simulations were carried out using the ABAQUS solver. Geometric nonlinearity was not considered, to simplify the analysis under the assumption of linear material behavior. The material properties assumed were an elastic modulus of 185 GPa and a Poisson's ratio of 0.3, typical for AISI 316L stainless steel under elastic deformation

conditions. The N4 and N12 finite element meshes are shown in Figure 4. Convergence of the mesh was performed, resulting in the N4 geometry meshed with 488083 C3D4 elements and the N12 geometry meshed with 720339 C3D4 elements, of approximate global size of 0.2 mm, and approximately 79 elements per circle, resulting in mesh represented on Figure 4.

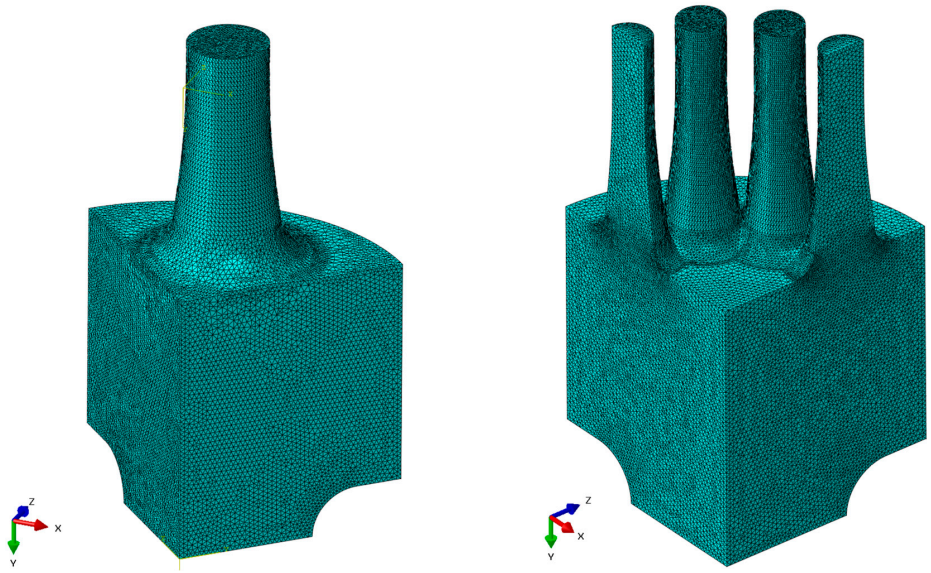

(**a**) (**b**)

Figure 4. Mesh of finite elements for (**a**) N4 geometry (**b**) N12 geometry.

FEA revealed that the region of highest stress concentration was in the middle part of both specimens. This is represented visually in Figure 5a for the N4 specimen and Figure 5b for the N12 specimen. The detailed analysis focused on this central region, comparing the computed stress values against the theoretical axial stress in the direction of loading, calculated from the uniform cross-sectional area of 38.1 mm^2.

The primary stress analysis in the middle part of each specimen revealed that the maximum Von Mises stress reached 266.1 MPa for the N4 specimen and 265.9 MPa for the N12 specimen. The maximum value of stress in the loading direction was observed as 267.5 MPa for the N4 specimen and 264.6 MPa for the N12 specimen. Subsequent evaluations at the midplane of the specimens assessed both the maximum and minimum stress levels, where the N4 specimen exhibited a maximum Von Mises stress of 263.3 MPa and a minimum of 262 MPa on the midplane. The corresponding axial stresses in the loading direction were 263.4 MPa and 262.1 MPa, with variations ranging from 0.1% to 0.4% relative to the theoretical stress. Comparison between the N4 and N12 specimens showed stress level differences ranging from 0.1% to 0.5%, underscoring the consistency across different specimen geometries. These results are summarized in Tables 2 and 3, which present a comparative analysis of the stress levels within the specimens under study. Stress distributions are visible in Figures 5–8 for both geometries.

Table 2. Comparison of Von Mises stress obtained by FEM.

Specimen	Von Mises (MPa) Global Maximum	Von Mises (MPa) Midplane Maximum	Von Mises (MPa) Midplane Minimum
N4	266.1	263.3	262.2
N12	265.9	264.6	261.1
Stress concentration N4/N12 (%)	0.08	−0.48	0.37

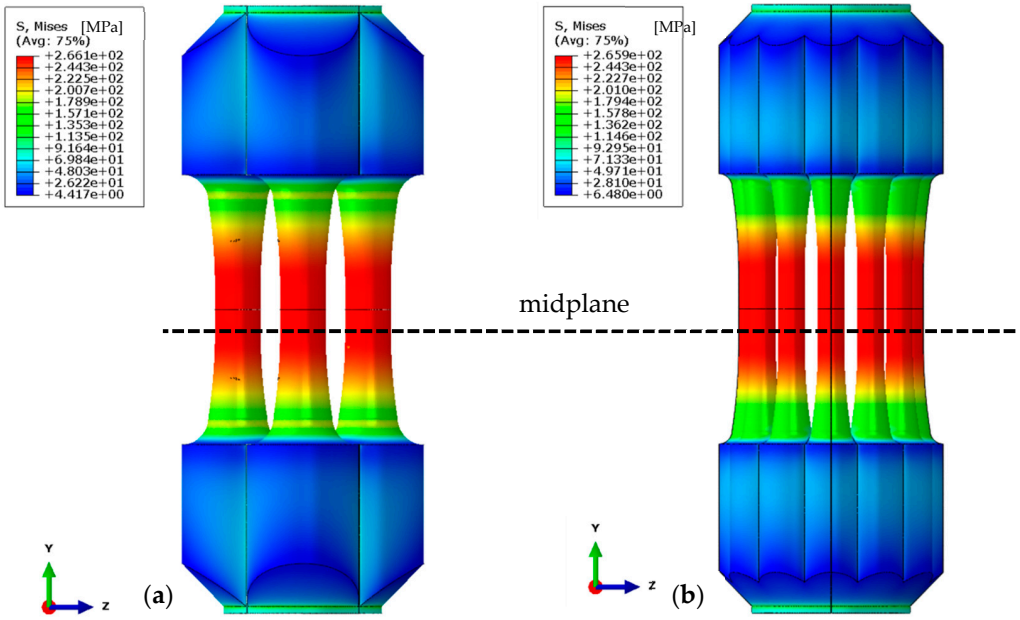

Figure 5. Von Misses stress values for (**a**) the N4 specimen (**b**) the N12 specimen.

Table 3. Comparison of axial stress in loading direction obtained by FEM.

Specimen	Axial Stress in Loading Direction (MPa) Global Maximum	Axial Stress in Loading Direction (MPa) Midplane Maximum	Axial Stress in Loading Direction (MPa) Midplane Minimum
N4	267.5	263.4	262.1
N12	267.1	264.6	261.1
Stress concentration N4/N12 (%)	0.15	−0.46	0.36

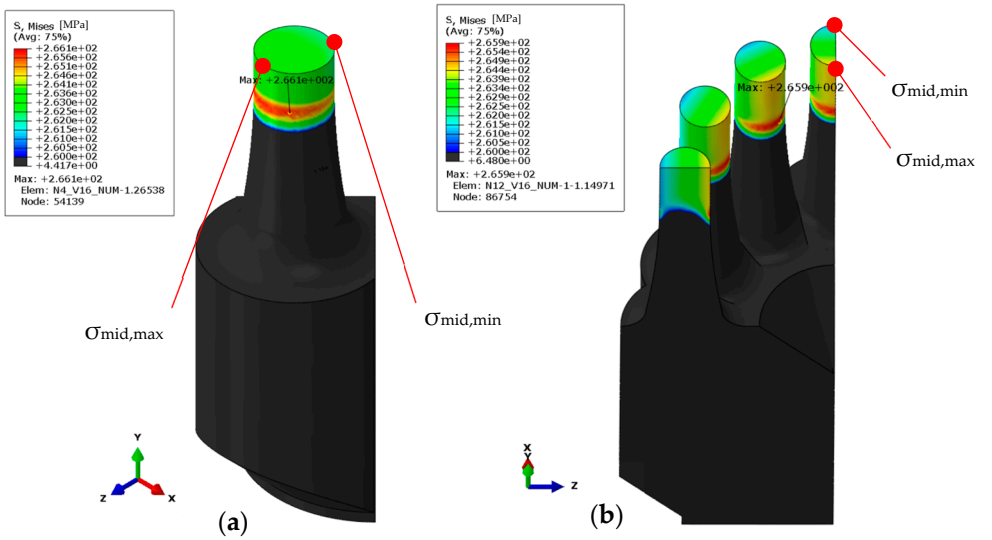

Figure 6. Maximum Von Misses stress values and positions of maximum and minimum values on the midplane for (**a**) the N4 specimen (**b**) the N12 specimen.

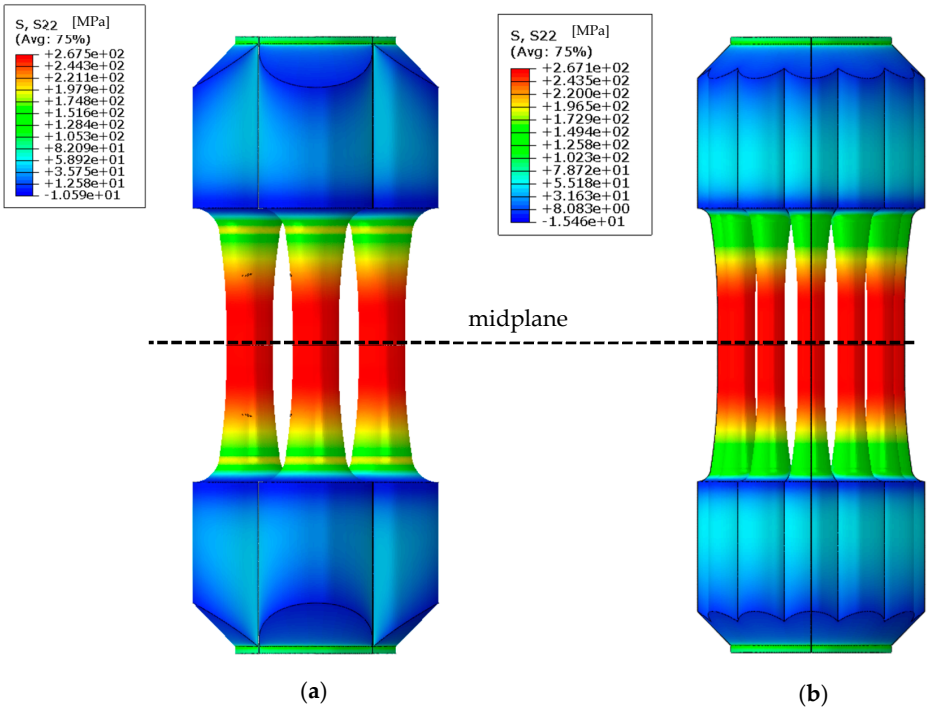

Figure 7. Maximum axial stress values in the direction of loading for (**a**) the N4 specimen (**b**) the N12 specimen.

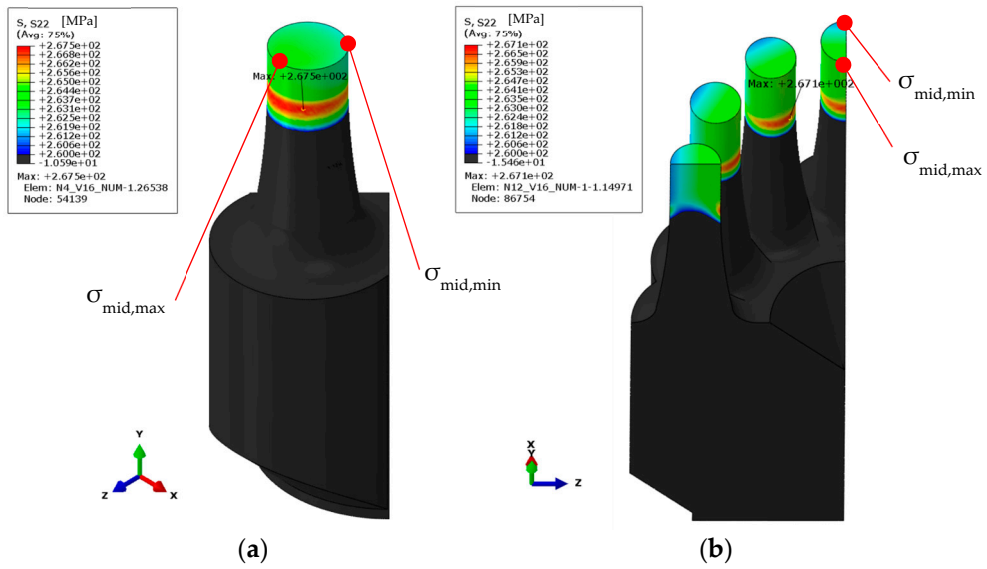

Figure 8. Maximum axial stress values in the direction of loading and positions of the maximum and minimum values on the midplane for (**a**) the N4 specimen (**b**) the N12 specimen.

2.2. Manufacturing and Powder Properties

The designed specimen geometries were fabricated precisely using the EOS M290 [39] machine, which utilizes laser powder bed fusion (LPBF) technology. Given the low slenderness ratio of the specimen, which was less than 8:1, a brush was recommended by the manufacturer for the application of material layers, each with a thickness of 0.04 mm. These layers were melted using a 214 W laser beam that travelled at a speed of 928 mm/s, with a hatch distance of 0.1 mm. For building the outer contours of the specimen, different parameters were employed compared to the infill. The laser power used for the contour was 136.1 W, with a laser speed of 446.9 mm/s and a layer thickness of 0.04 mm. The use of two different printing parameters is visible in Figure 9, where the green lines represent the

direction of laser travel for one of the layers inside of the printed area and the purple lines represent laser travel, where the contours' printing parameters were used.

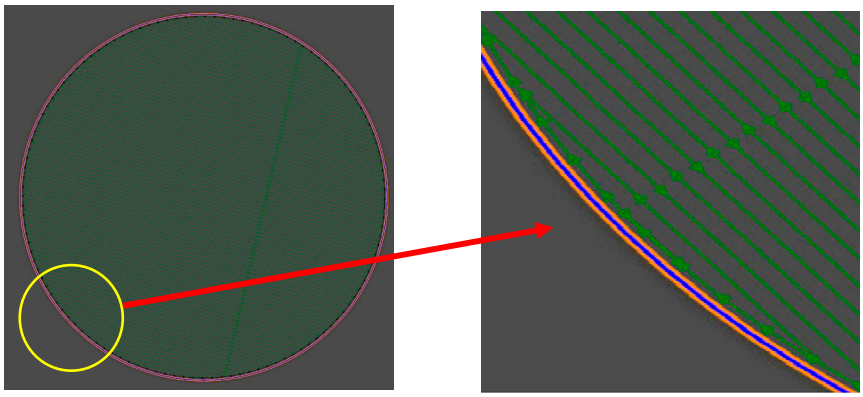

(**a**) (**b**)

Figure 9. (**a**) Laser travel path on one rod (**b**) detailed laser travel path on the edge of one rod.

Additionally, the process involved rotating the angle of the laser beam after each layer to prevent overlapping of the melt paths, enhancing the uniformity and quality of the build. At a layer height of 0.04 mm, the laser starts at an angle of 0°. For the subsequent layers, the laser rotates by 47° increments, exposing at angles of 47°, 94°, and 141°, and continuing in this pattern. This rotation method ensures that the exposure angles vary with each layer, reducing the risk of defects due to overlapping. However, there is a specific range of angles at which the laser does not expose because the direction of the protective gas flow would be suboptimal within this range. Generally, the system is designed to rotate consistently according to the specified schedule to ensure the optimal material properties and structural integrity of the manufactured parts.

The specimens, including tensile specimens and both N4 and N12 configurations, were arranged on the printing tables as indicated in Figure 10. All the geometries were printed in a single production cycle to maintain uniformity in the printing process. The direction of printing for these specimens is specified in Figure 11. Following the printing process, the specimens were detached from the printing table, and their manufactured geometries are displayed in Figure 11, with the build direction also marked.

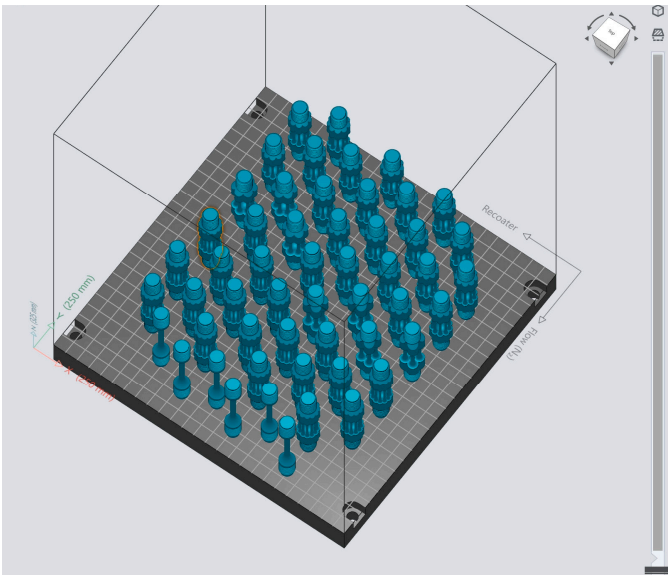

Figure 10. Arrangement of specimens on the printing table.

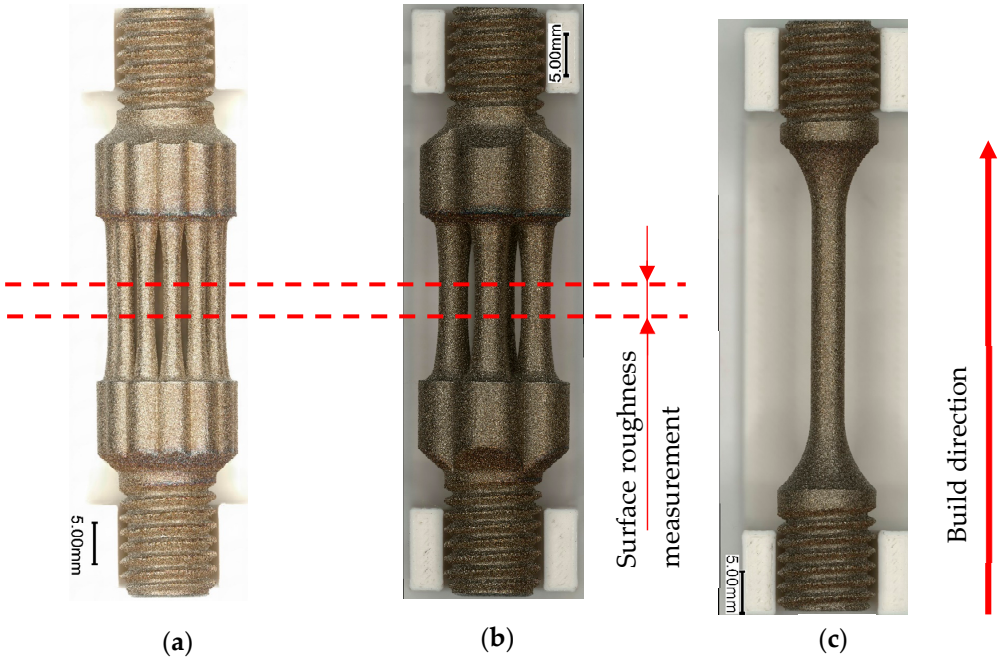

Figure 11. Manufactured specimens with (**a**) N12 specimen geometry (**b**) N4 specimen geometry (**c**) tensile specimen geometry.

In alignment with the research focus on untreated surfaces, no post-production treatments were applied to the specimens. They were maintained in their as-printed state to preserve their manufactured characteristics and surface roughness from the additive manufacturing process. Threads were also produced concurrently at the ends of the specimens, with the main bodies using the additive manufacturing process. This integrated approach facilitated the investigation of the mechanical properties and fatigue behavior of the specimens without any alterations that could arise from post-processing.

The specimens were manufactured using M4P™ 316L austenitic steel (1.4404). The chemical composition of this material, including the maximum and minimum percentages of each element as guaranteed by the manufacturer, is listed in Table 4. Prior to the delivery of the material, the specific chemical composition of the batch used for manufacturing the specimens was verified through chemical analysis.

This analysis was conducted in accordance with ISO 15350 [40], which determines the weight percentage of carbon, and the inductively coupled plasma optical emission spectroscopy (ICP-OES) method was used for quantifying all the other elements, as detailed in Table 4.

Table 4. Chemical composition of M4P™ 316L [41].

Element	C	Si	Mn	Cr	Ni	Mo
Min (%)	-	-	-	16	10.5	2
Max (%)	0.03	1	2	18	14	3
Batch (%)	0.02	0.6	0.9	16.9	12.2	2.6
Standard	ICP-OES	ICP-OES	ICP-OES	ICP-OES	ICP-OES	ISO 15350

The physical properties of the material were characterized by the manufacturer, including the particle size distribution, which is detailed in Table 5. The average size of 90% of the particles was reported as 45 µm. Although the manufacturer provides typical mechanical properties derived from tensile tests, these values were not obtained from the batch used to manufacture the specimens and should be verified through in-house tensile testing.

Table 5. Powder size distribution.

Characteristic	d10 (µm) (xc min) (%)	d50 (µm) (xc min) (%)	d90 (µm) (xc min) (%)	−15 µm (xc min) (%)	+45 µm (xc min) (%)
Min	16	26	40	-	-
Max	26	36	50	5	5
Batch	20	32	45	2.8	2.6
Standard	ISO 13322-2	ISO 13322-2	ISO 13322-2	ISO 13322-2	ISO 4497

2.3. Tensile Properties

The quasi-static tensile properties were evaluated using three tensile specimens subjected to tensile testing on an MTS LANDMARK 370.1 servo-hydraulic machine. A mechanical extensometer, MTS 634.12F-25, was used to measure strain during the tests, as shown in Figure 12. The tensile tests were conducted under controlled displacement settings on the MTS machine, with a strain rate of 0.00025 strain/s up to the point of yield strength, which was then increased to 0.002 strain/s until fracture occurred.

Figure 12. Mounting of the extensometer on a tensile specimen.

The tensile material properties were assessed in compliance with the ISO 6892-1 Standard [42] on testing of tensile specimens, ensuring the reliability and standardization of the testing process. To mitigate any potential misalignment caused by the clamping of the specimens, a cardan joint was incorporated between the tensile specimens and the upper clamps of the testing machine. This setup helped in maintaining the integrity of the loading path and ensured accurate measurement of the material's mechanical properties.

The provided material properties, including tensile strength, yield strength, and elongation at break, assume a relative density of 99.95% and are summarized in Table 6. It should be noted that the manufacturer did not specify the parameters of tensile tests for metal powder.

Table 6. Tensile powder and specimen properties at room temperature.

Material		Ultimate Tensile Strength (MPa)	Yield Stress (MPa)	Elongation (%)
Metal powder [41] *		574	428	52
Tensile test	min	600	464	75
	max	613	487	67

* M4P™ 316L austenitic steel (1.4404).

The representative engineering stress vs. strain curve response of the tensile specimens is displayed in Figure 13. The tensile properties such as yield strength, ultimate tensile strength, and elongation at break were obtained from tensile tests and are listed in Table 6. Comparing the tensile properties shows that the ultimate yield stress and yield stress are comparable between the tensile specimens and powder, with the ultimate yield stress increasing by about 5% to 603 MPa, and the yield stress increasing by about 8.4% to 464 MPa. However, the elongation at break increased by around 38% with the tensile test compared with the data provided for bulk powder. Differences could occur due to a different strain rate of the tensile tests, which was not provided for the powder properties tests. However, comparing the AM tested tensile specimens to commercial sheet material in annealed condition [43] showed that the AM material had higher yield stress and elongation at break due to remelting and deposition, which altered the material properties, resulting in a ductile fracture of the tensile specimen, as shown in Figure 14.

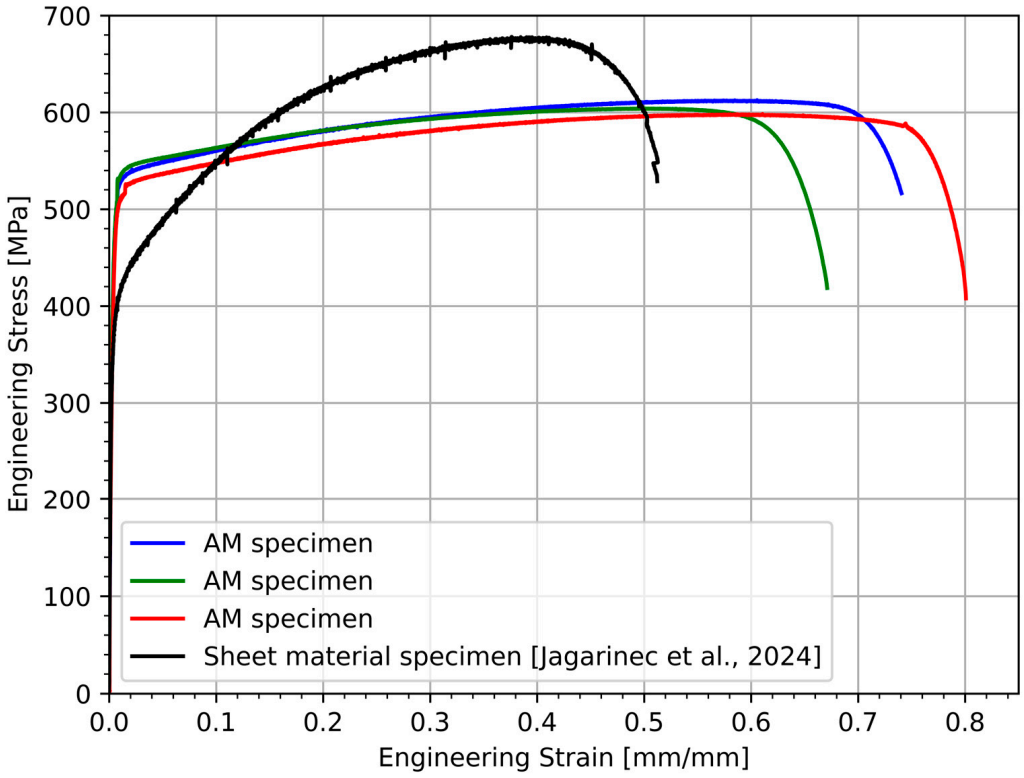

Figure 13. Tensile test engineering stress vs. engineering strain curves by comparing the rolled AISI 316L, data from [43].

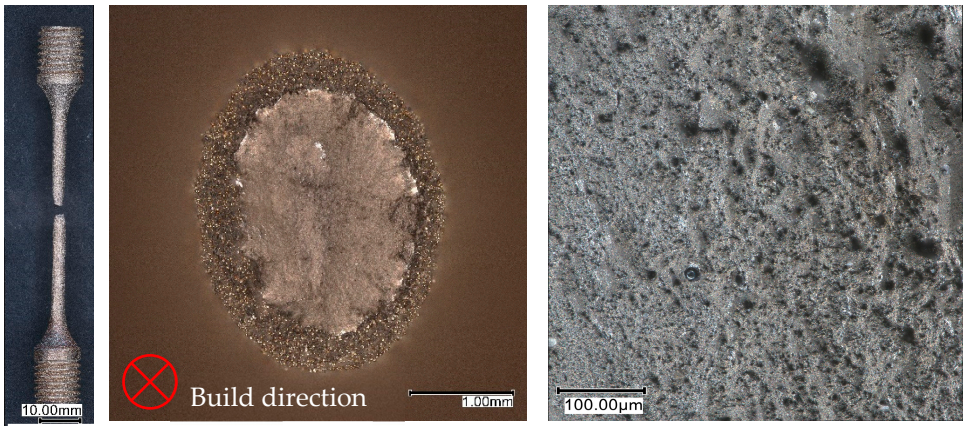

Figure 14. Fracture surface of the tensile test specimen: (**a**) specimen after tensile test, (**b**) fracture surface, (**c**) detailed part of the fractured surface.

2.4. Surface Roughness

Surface roughness measurements were conducted on both the tensile and fatigue specimens to assess the quality of the surfaces produced by the additive manufacturing process. A Keyence VHX-7100 microscope, employing 1000× magnification, was utilized to examine the surface area of the main part of each specimen closely. The specific areas under examination are highlighted in Figure 15. Each line present roughness measured path, and average values of all colored lines are used for roughness relevant value.

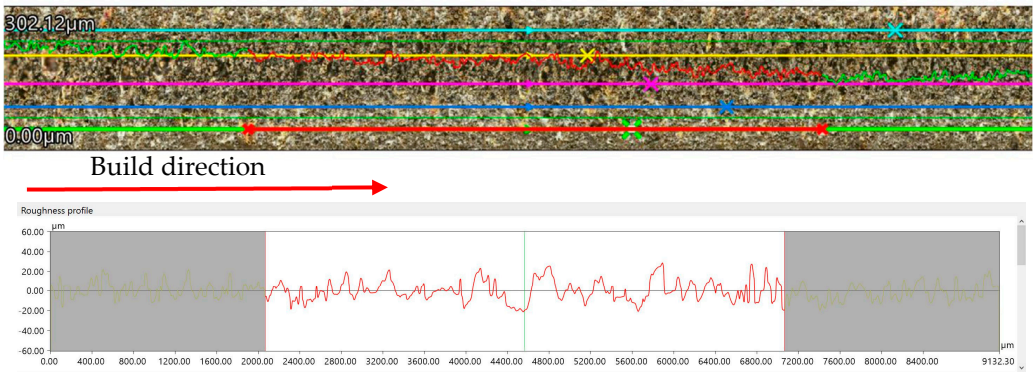

Figure 15. Measurements of the surface roughness with the Keyence VHX-7100.

A total of five measurements of roughness were taken for each specimen. These measurements employed filters with a cut-off length (λc) of 2.5 mm and a short wavelength cut-off (λs) of 8 µm, in accordance with ISO 21920-3 [44]. To ensure accuracy and relevance to the layering process inherent in additive manufacturing, measurements were performed perpendicular to the orientation of the layers, as depicted in Figure 11. As shown in Table 7, the surface roughness of tensile specimens was not significantly different than the surface roughness of the specimens for fatigue testing, with the Ra of the tensile specimens being 9.5 µm and that of the fatigue specimen being 9.7 µm. Furthermore, the geometries of both fatigue specimens (N4 and N12) had similar surface roughness.

Table 7. Measured surface roughness.

Specimen Geometry	Average Ra (μm)	St. Dev (μm)
N4	9.752	1.076
N12	9.766	1.274
Tensile	9.544	0.604

2.5. Microstructure and Porosity

The Archimedes method was employed to determine the density of each specimen, with three measurements taken for each specimen to ensure accuracy. These measurements were then compared to assess any deviations that might indicate porosity or other anomalies related to the additive manufacturing process. The measured density obtained with the Archimedes method showed similar density for both the N4 and N12 specimens, with a difference of around 0.3%. The density of the N4 specimen was measured at 7.8433 g/cm^3 and the density of the N12 specimen at 7.8667 g/cm^3.

To examine the microstructure, the specimens were sectioned using wire erosion, a process that provides a clean cut without altering the material properties by thermal effects. This method was crucial for obtaining an unchanged surface in the middle part of each specimen that represents the internal structure accurately. After sectioning, the specimens were prepared for microscopic examination. This preparation involved grinding the surfaces to achieve a uniform flatness, followed by etching with a solution composed of 5 g of FeCl2, 10 mL of HCl, and 100 mL of ethanol. This etching process revealed the underlying microstructure by corroding phases selectively at different rates, enhancing the visibility of the grain boundaries and any microstructural defects. The treated surfaces were then examined under a Keyence VHX-7100 microscope.

Microhardness measurements were performed on the treated surfaces to assess the material hardness variations from the outer surface inward. Using a Vickers hardness tester (HV0.1), the measurements were taken systematically at intervals of 0.15 mm. To compare the Vickers hardness values of both specimens, the positions of the measurements were normalized to the distance from the outer surface relative to the diameter of the rod on which the measurements were performed.

The initial imprint of the HV measurements, visible in Figure 16, marks the start of a series of hardness tests whose results are compiled in Figure 17. The Vickers hardness tests showed comparable values across the specimens in both the perpendicular and parallel directions relative to the build plate. However, variations in hardness are evident and depend significantly on the position within the specimen where each measurement was taken, while variations were higher in the parallel direction of measurement.

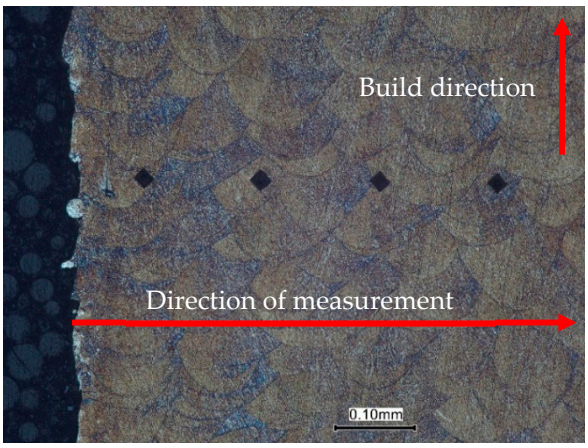

Figure 16. Positions of Vickers hardness measurements.

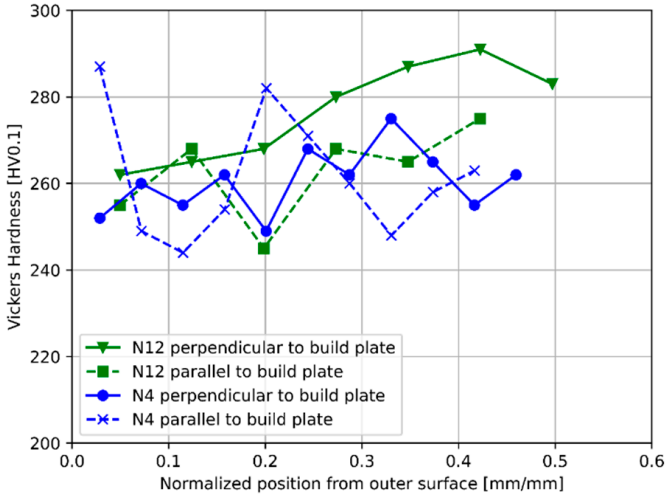

Figure 17. Vickers hardness measurements.

The microstructure of a rod of the N4 specimen in parallel direction to the build layers is detailed in Figure 18a. The cross section revealed the directional characteristics of the laser travel during manufacturing. Three distinct directions of laser travel are evident, corresponding to the layer-by-layer additive manufacturing process. The outer surface of the rod showcased a consistently melted layer of approximately 0.1 mm thickness, aligning with the hatch distance settings used during the specimen's fabrication.

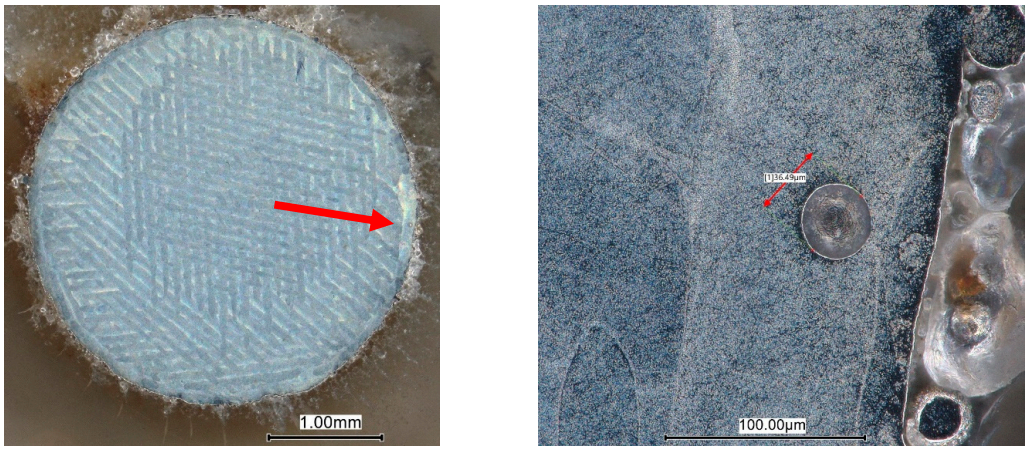

(**a**) (**b**)

Figure 18. Structure and defects in the N4 specimen in the layer build direction: (**a**) cross section of one rod, (**b**) material defect near the surface. Arrow at (**a**) shows detail at (**b**).

Despite the overall integrity of the microstructure, minor defects are observed within the cross section. More notably, larger defects are located predominantly in the outer layer of the rod. These defects, which could potentially influence the mechanical properties, are detailed in Figure 18b. One significant defect, characterized by its nearly circular shape with a diameter of approximately 36.5 µm, is encapsulated entirely by the surrounding melted material, highlighting the complexities and challenges in controlling material behavior during the additive manufacturing process.

The microstructural characteristics were assessed from a perpendicular view relative to the layer build direction, as depicted in Figure 19a. This analysis revealed distinct melting pools corresponding to each pass of the laser, providing insight into the layer-wise construction of the specimen. The outer two layers are notably darker, a consequence of

the laser travel history, which affects the thermal characteristics and material response in these regions.

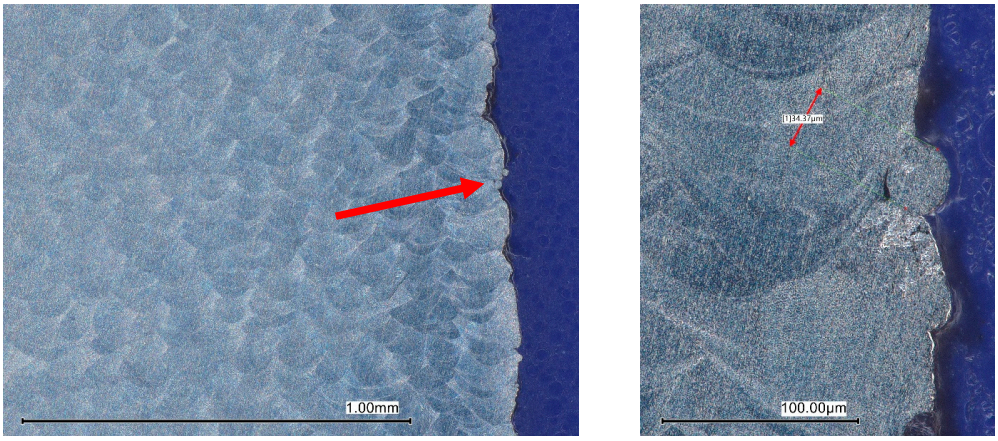

(**a**) (**b**)

Figure 19. Structure and defects in the N4 specimen perpendicular to the layer build direction. Arrow at (**a**) shows detail at (**b**).

The outer surface is uneven, featuring notches that disrupt the uniformity of the layer interface, with a prominent notch highlighted in Figure 19a. Additionally, Figure 19b shows a partially melted powder particle, approximately 34.4 µm in size. This particle is separated distinctively from the surrounding material, with visible pores indicating incomplete fusion.

The microstructural analysis of the N12 specimen, shown in Figure 20a, reveals a pattern similar to that observed in the N4 specimen, with four distinctive directions of laser travel evident. This similarity underscores the consistent layering technique used across different specimen geometries. Upon further magnification, various defects became apparent within the cross section, particularly a larger defect located in the outer layer of the melted material, similar in shape and size to that observed in the N4 specimen. This defect is depicted in Figure 20b where, due to the lighting conditions during imaging, the boundaries of solidification pools across different layers are distinctly visible, providing further insight into the layer-by-layer manufacturing process.

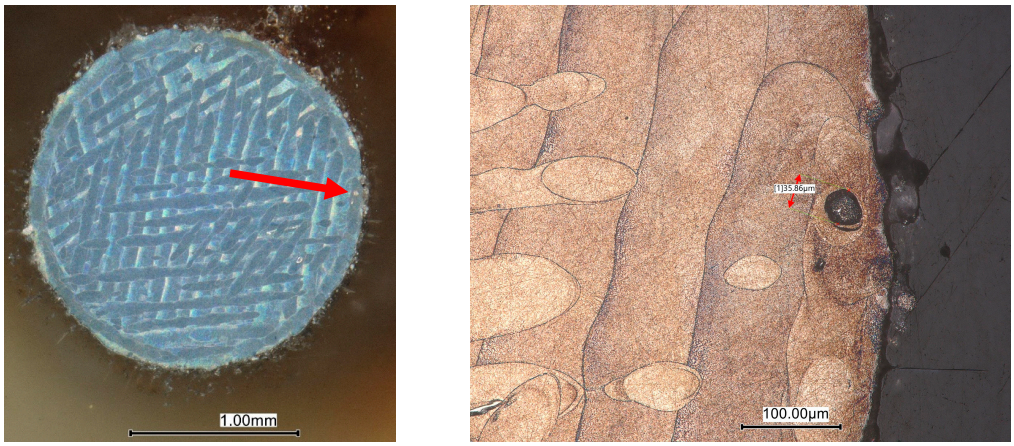

(**a**) (**b**)

Figure 20. Structure and defects in the N12 specimen in the layer build direction. Arrow at (**a**) shows detail at (**b**).

A perpendicular view of the N12 specimen, presented in Figure 21a, mirrors observations from the N4 specimen. Notches are clearly visible on the outer surface of the specimen, suggesting irregularities during the laser melting process. Figure 21b highlights a subsurface defect, nearly circular in shape, which is likely attributable to trapped gas during the manufacturing process.

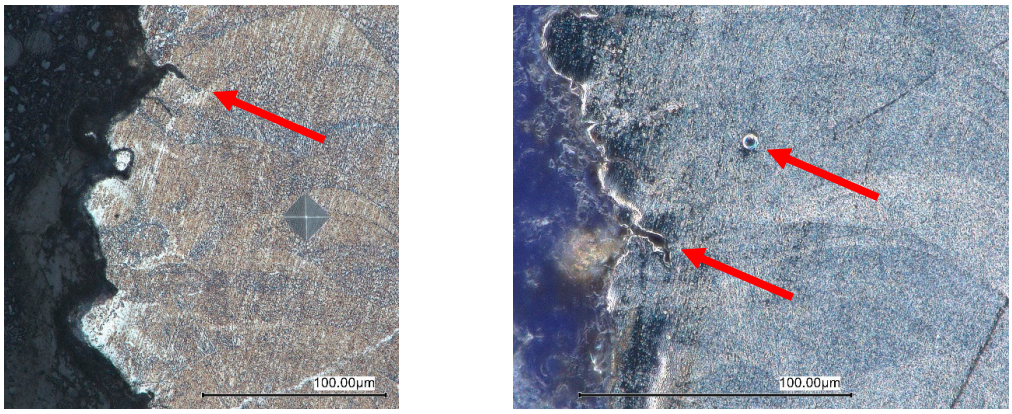

(**a**) (**b**)

Figure 21. Structure and defects in the N4 specimen perpendicular to the layer build direction. Arrow at (**a**) shows detail at (**b**).

3. Results

3.1. High Cycle Fatigue Test

Fatigue testing was conducted on the N4 and N12 specimens using MTS LANDMARK 370.1 servo hydraulic machines. Throughout the tests, the loading force and displacement of the actuator were captured at each peak and trough of the force sinusoids. This was performed in order to reduce the recorded data during fatigue testing, as a change in displacement is most visible at maximum loading force. The recorded displacement of each cycle allows estimation of the number of cycles when the first rod of the specimen fails, as the stiffness of the specimen will change with the fatigue crack propagation through the rod. Figure 22 shows a change in the displacement of the actuator on the N4 specimen that was tested at a maximum stress level of 280 MPa, where the change in displacement is visible at around 7×10^5 cycles, when crack propagation occurred on the first rod. After the failure of the first rod, displacement was almost constant, and it was increasing slowly as the crack initiated in the second rod. The fatigue crack in second rod started to propagate rapidly at around 7.5×10^5 cycles until the specimen failed. The cycles of final failure were used for establishing the S–N curves.

The testing was controlled by a force with a stress ratio (R) of 0.1 calculated by Equation (1), at a frequency of 15 Hz, conducted at an ambient temperature across various loading force levels. The specimens were subjected to cyclic loading under different stress levels calculated by Equation (2) until complete failure occurred, characterized by the failure of all the rods in a specimen. The specimens that endured up to 2×10^6 cycles were classified as runouts and were not subjected to further testing until failure.

$$R = \frac{F_{min}}{F_{max}} = 0.1 \tag{1}$$

$$\sigma_{max} = \frac{F_{max}}{A_4 \cdot 4} = \frac{F_{max}}{A_{12} \cdot 12} \tag{2}$$

A cardan joint with clearance fit was utilized between a specimen and the upper clamps of the MTS machine, as depicted in Figure 23. The cardan joint was used to achieve alignment of the specimen's symmetry line with the load direction of the MTS machine. This setup helped in mitigating any potential misalignment issues due to the manufacturing

process that could affect the test results due to uneven stress distribution in the tested specimen, as it reduces bending of the tested specimen.

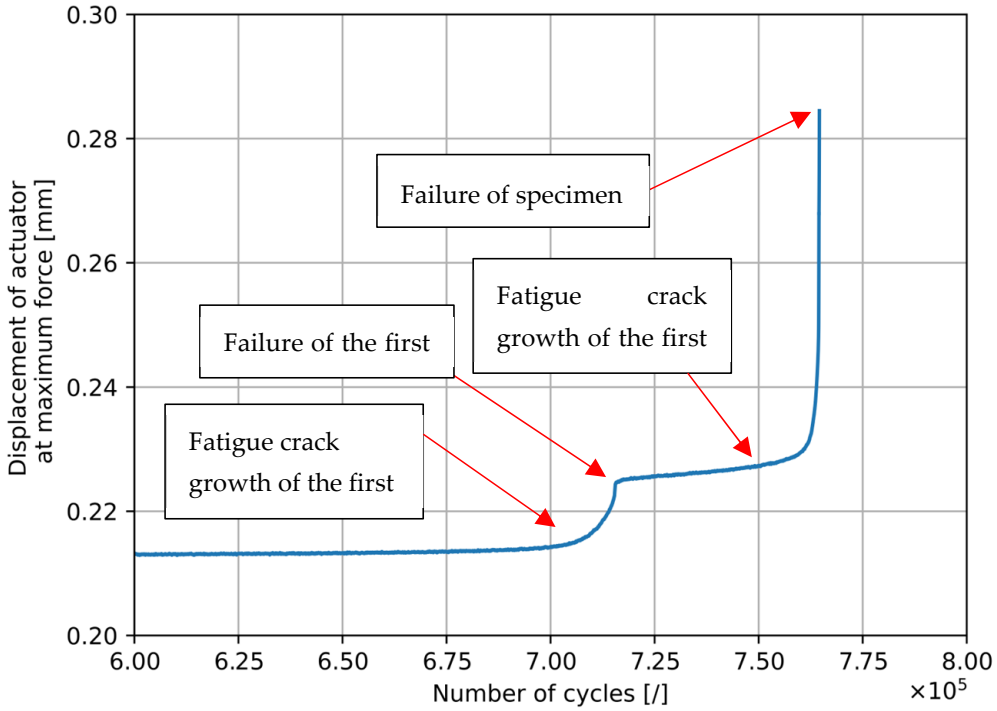

Figure 22. Measured displacements of the actuator during the fatigue test of specimen N4 tested at a maximum stress of 280 MPa.

(**a**) (**b**)

Figure 23. Clamping and fixtures of specimens for fatigue testing (**a**) the N12 specimen and (**b**) the N4 specimen.

The fatigue test results for both the N4 and N12 specimens are illustrated in Figure 24, where the S–N curves were constructed to depict the relationship between stress levels and the number of cycles to failure. The N4 specimens endured more cycles at a given stress level consistently compared to the N12 specimens, indicating better fatigue resistance. However, it was noted that the scatter in the number of cycles increased as the stress decreased across both geometries. The divergence in cycle numbers between the two specimen types was most pronounced at lower stress levels. At higher stress levels, particularly at 420 MPa, the results for both the N4 and N12 specimens showed comparable numbers of cycles, with overlapping data points indicating similar fatigue behavior.

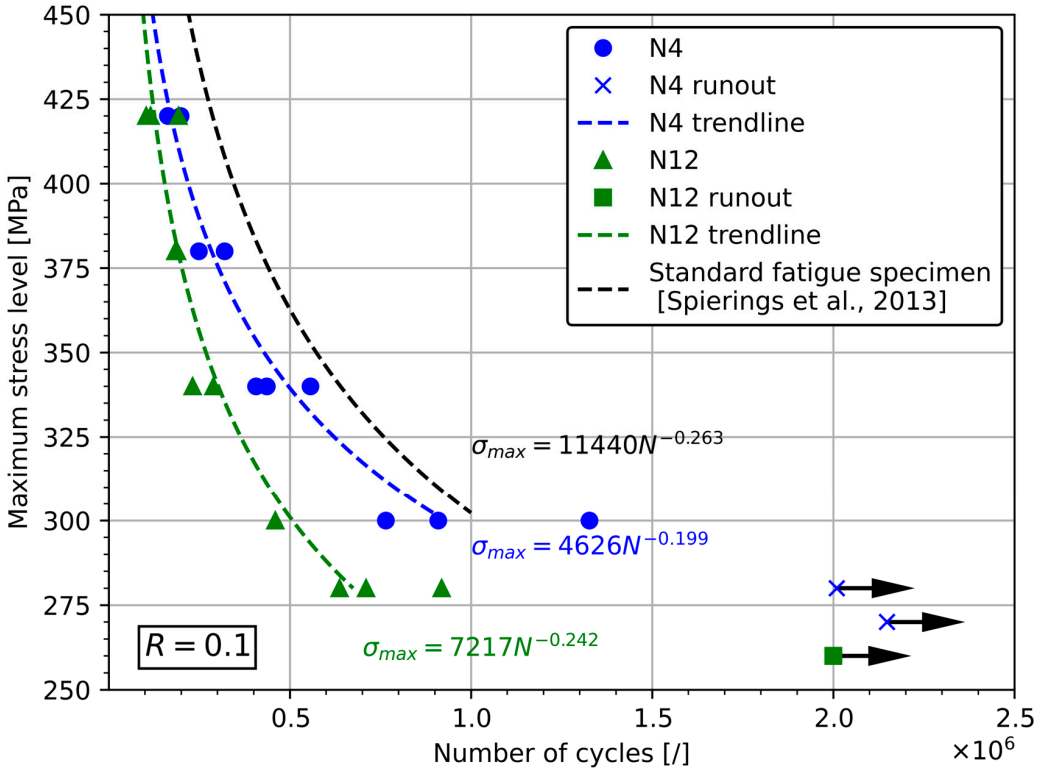

Figure 24. S–N curves for the N4 and N12 tested geometries by comparing the rolled AISI 316L, data from [35].

At the maximum stress level tested, 280 MPa, two N4 specimens were subjected to fatigue testing. Interestingly, one of these N4 specimens did not fail, and the fatigue test was terminated, whereas the other failed after 1.1×10^6 cycles. To explore the endurance threshold further, another N4 specimen was tested at a slightly reduced stress level of 270 MPa and did not fail, even after 2×10^6 cycles. In contrast, the N12 specimens tested at 280 MPa failed before reaching 1×10^6 cycles. For the N12 specimens to achieve over 2×10^6 cycles, the stress level had to be reduced to 260 MPa. Although there are insufficient data to confirm the fatigue limits for both geometries statistically, the available results suggest that the fatigue limit of N4 specimens might be higher than that of N12 specimens. However, comparing the results of fatigue testing with other studies of additive manufactured AISI 316 standard fatigue specimens tested in the as-built state at a loading ratio of R = 0.1 yielded similar results [35,45].

3.2. Fractography

Fractographic analyses were conducted on the fatigue fracture surfaces of both the N4 and N12 specimens, which were tested at maximum stresses of 420 MPa and 280 MPa. The locations of fracture surfaces on the specimens are visible in Figure 25. All failures of rods occurred in the middle part of the specimens, around the location of the maximum stress

values. The analysis of an N4 specimen tested at 420 MPa, which endured 198,184 cycles until failure, is detailed in Figure 26. A global examination of the crack surface, visible in Figure 26a, reveals that, in the marked rod, the failure was due predominantly to fatigue. This is based on a comparison with surfaces of other rods on this specimen. The surface where the fatigue crack growth occurred maintained its nearly circular original manufactured shape, indicating minimal plastic deformation. In contrast, the originally circular shape was distorted in the other rods, indicating that the rods failed due to the material reaching its ultimate tensile strength due to higher stress values and not due to fatigue crack propagation through the rod. However, even among the rods with extensive deformation, areas with brighter surfaces are evident (indicated by the arrows), signifying regions where fatigue cracks initiated and propagated partially. A rod characterized entirely by fatigue failure was scrutinized under higher magnification to pinpoint the crack initiation site and to examine the surface details more closely. The primary crack initiation site was identified within a rectangular marker in Figure 26b. Further magnification of this area, indicated by a blue arrow, reveals the crack initiation site in greater detail (Figure 26c,d), showing that the fatigue crack initiated at the surface and propagated into the rod in a roughly elliptical pattern. Notably, the expected geometry of the outer surface, based on predefined specifications, should be circular. However, at this level of magnification, irregularities are apparent; the surface exhibits indentations inward at the crack initiation site, deviating from the intended circular geometry.

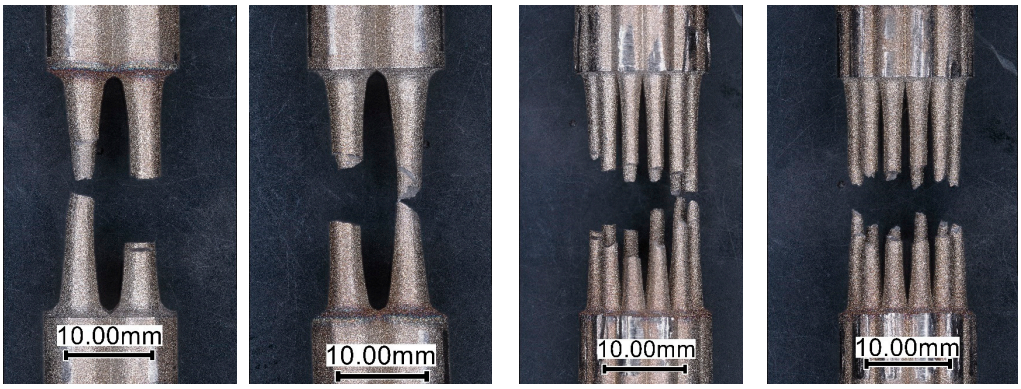

Figure 25. Failure of fatigue tested specimens at R = 0.1: (**a**) the N4 specimen at maximum stress of 280 MPa, (**b**) the N4 specimen at maximum stress of 420 MPa, (**c**) the N12 specimen at maximum stress of 280 MPa, (**d**) the N12 specimen at maximum stress of 420 MPa.

The fractographic examination of an N4 specimen, which endured 1,168,512 cycles and was tested at 280 MPa, is detailed in Figure 27. The rods through which the crack propagated fully are marked with rectangles in Figure 27a, while a rod where the crack propagated until the specimen's failure is indicated by an arrow. In the rods exhibiting complete fatigue crack propagation, the initiation sites of the cracks are clearly visible and marked with arrows in Figure 27b,e. Consistently, these cracks originated from the surface, where irregularities are evident in the surface geometry at the initiation sites. Furthermore, within the interior of the rods characterized by fatigue surfaces, pores were observed which consist of unmelted material. Several of these pores are identified in Figure 27b–d, with arrows inside of the specimen highlighting the presence of pores and potential influence on the material's fatigue behavior.

The fracture surface of the N12 specimen subjected to a stress of 420 MPa is presented in Figure 28. The surfaces where the fatigue crack propagated fully are outlined in Figure 28a, distinguished by rectangles. The arrows point to areas where the fatigue crack initiated and propagated until the specimen ultimately failed. The initial crack sites on the rods where full fatigue crack propagation occurred are marked prominently with arrows in

Figure 28b–d, on the edges of surfaces, indicating that these cracks also initiated at the surface. Surface irregularities at these initiation sites are clearly visible, suggesting that such imperfections may play a significant role in the initiation and propagation of fatigue cracks. Inside of the rods affected by fatigue, visible change of the surface was detected, marked by arrows. Inside of the pores, a distinctive pattern is visible that could be connected to the manufacturing process and laser travel direction. The surface pattern of the pores shows parallel lines, similar to laser travel.

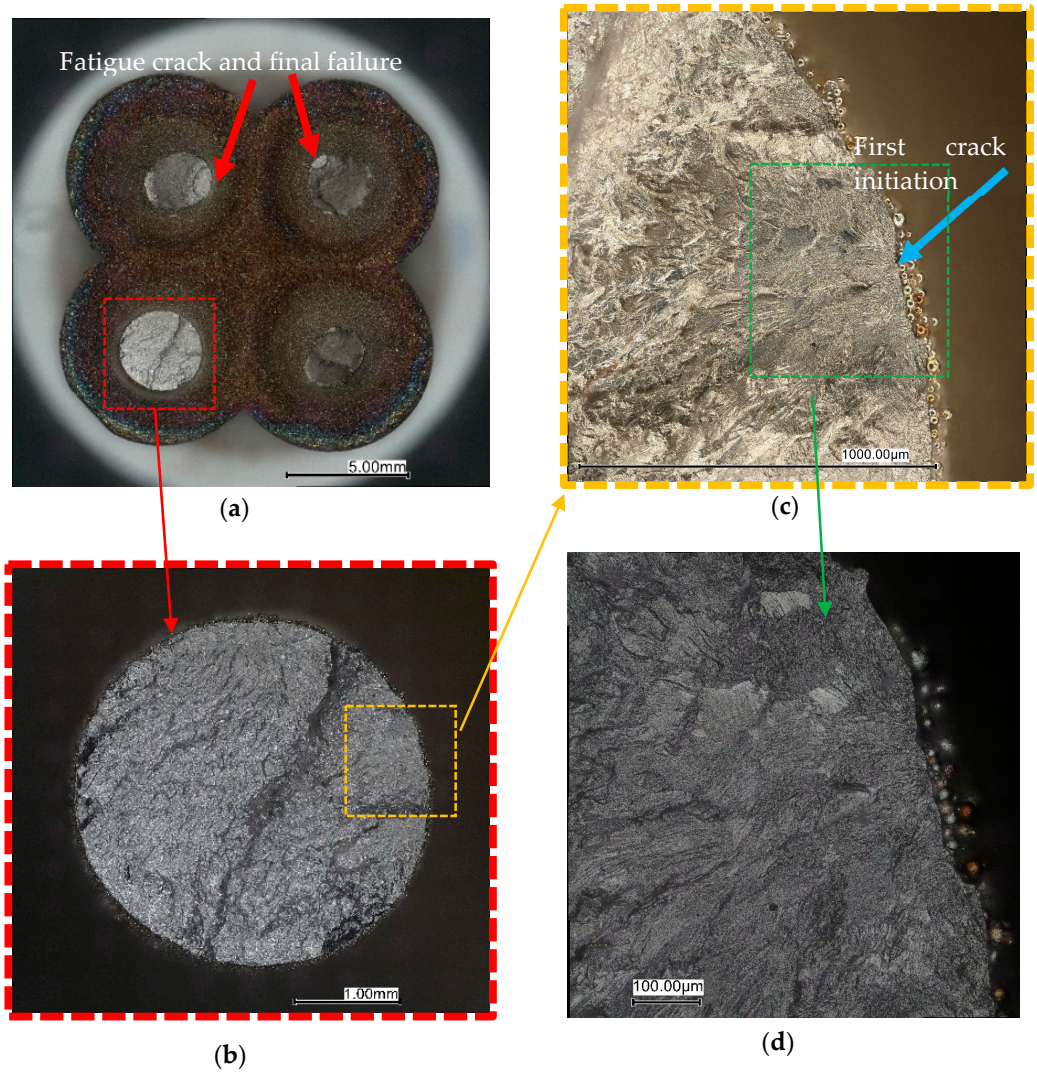

Figure 26. Fracture surface of the N4 geometry tested at a maximum stress level of 420 MPa: (**a**) fracture surface after the fatigue test, (**b**) the first rod fracture surface, (**c**) the first fatigue crack initiation site, (**d**) the surface defect at first fatigue crack initiation.

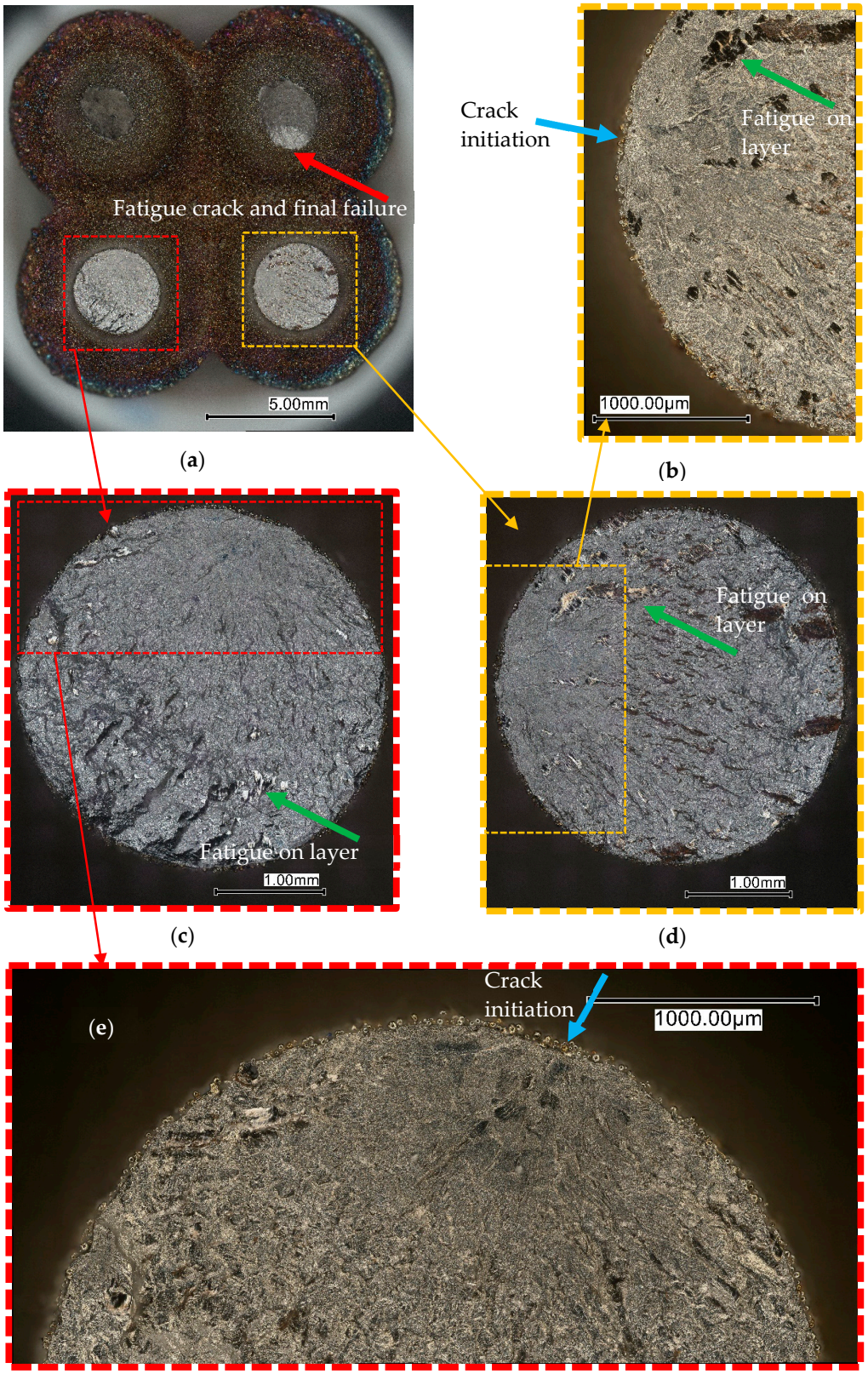

Figure 27. Fracture surface of the N4 geometry tested at a maximum stress level of 280 MPa: (**a**) fracture surface after the fatigue test, (**b**) the first fatigue crack initiation site, (**c**) the second rod fracture surface, (**d**) the first rod fracture surface, (**e**) the second rod fatigue crack initiation side. The red arrow in (**a**) shows details in (**c**), while the yellow arrow in (**a**) shows details in (**d**). The red arrow in (**c**) shows the detail in (**e**) where the fatigue crack has initiated.

The N12 specimen tested at 280 MPa is illustrated in Figure 29, where its fracture surfaces are displayed prominently. Crack initiation sites, from which the fatigue cracks propagated, are clearly visible on the rods and are indicated with arrows in Figure 29b,f. Notably, on a rod in Figure 29e, there is a discernible transition from high cycle fatigue (HCF) to low cycle fatigue (LCF) and plastic deformation. Initially, during the crack initiation phase, the rod maintained its circular shape, indicating it was under high-cycle-fatigue conditions. As the crack advanced toward the top right corner of the rod, the fatigue regime shifted from HCF to LCF, evidenced by a noticeable deformation from the original circular shape and alterations in the fracture surface. On fatigue crack growth surfaces, distinctive areas are visible, marked with arrows in Figure 29b,d,f, where the crack propagated on the boundary between two melted pools of material. Again, in these areas, the direction of laser travel is visible.

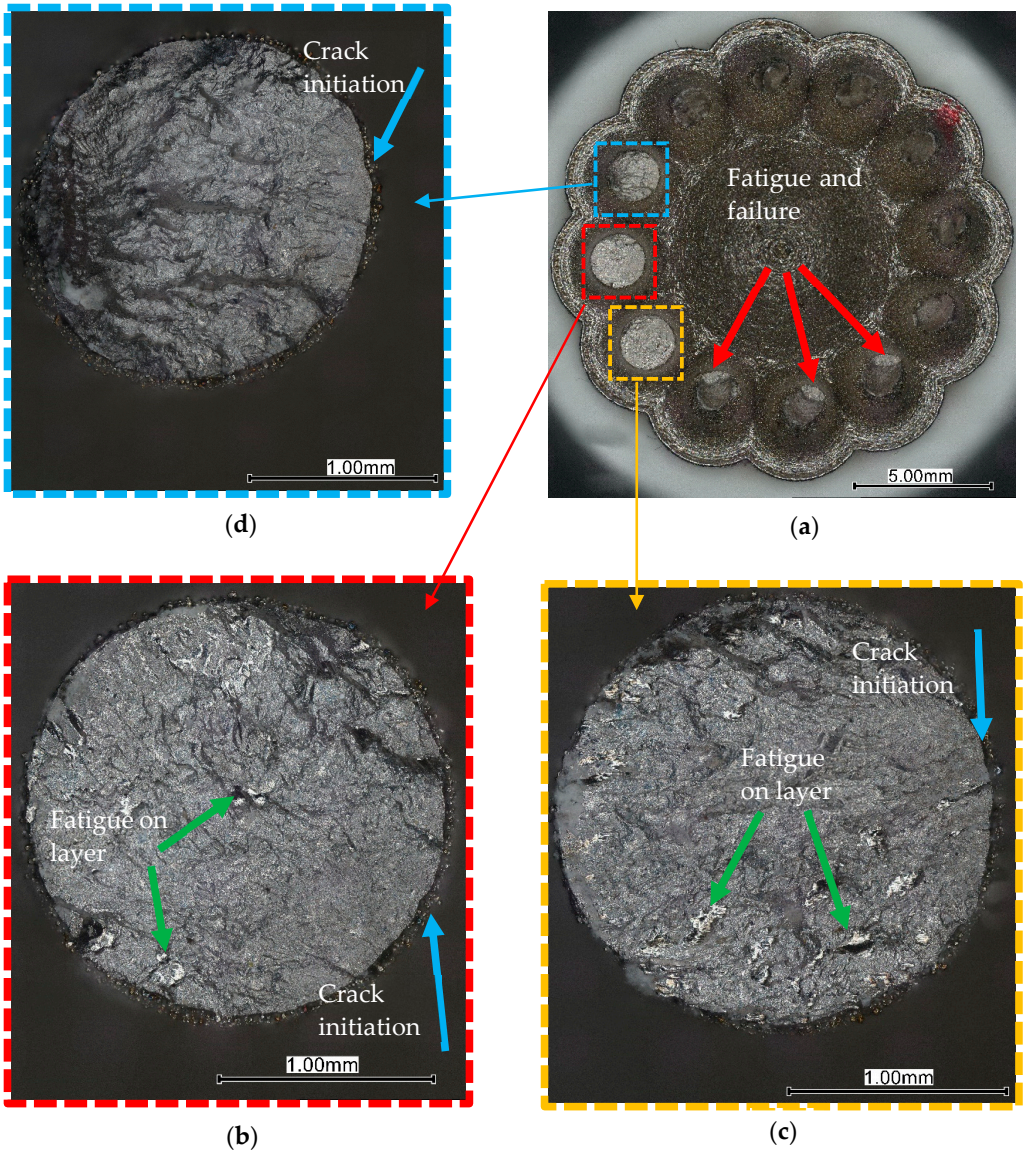

Figure 28. Fracture surface of the N12 geometry tested at a maximum stress level of 420 MPa: (**a**) fracture surface after the fatigue test, (**b**) the first rod fatigue fracture surface, (**c**) the second rod fatigue fracture surface, (**d**) the third rod fatigue fracture surface. The blue arrow in (**a**) shows the broken rod in (**d**), while the yellow arrow in (**a**) shows the detail in (**c**). The green arrows in (**b**,**c**) show fatigue at the place, where the blue arrow shows the initiation of a crack on the bar surface.

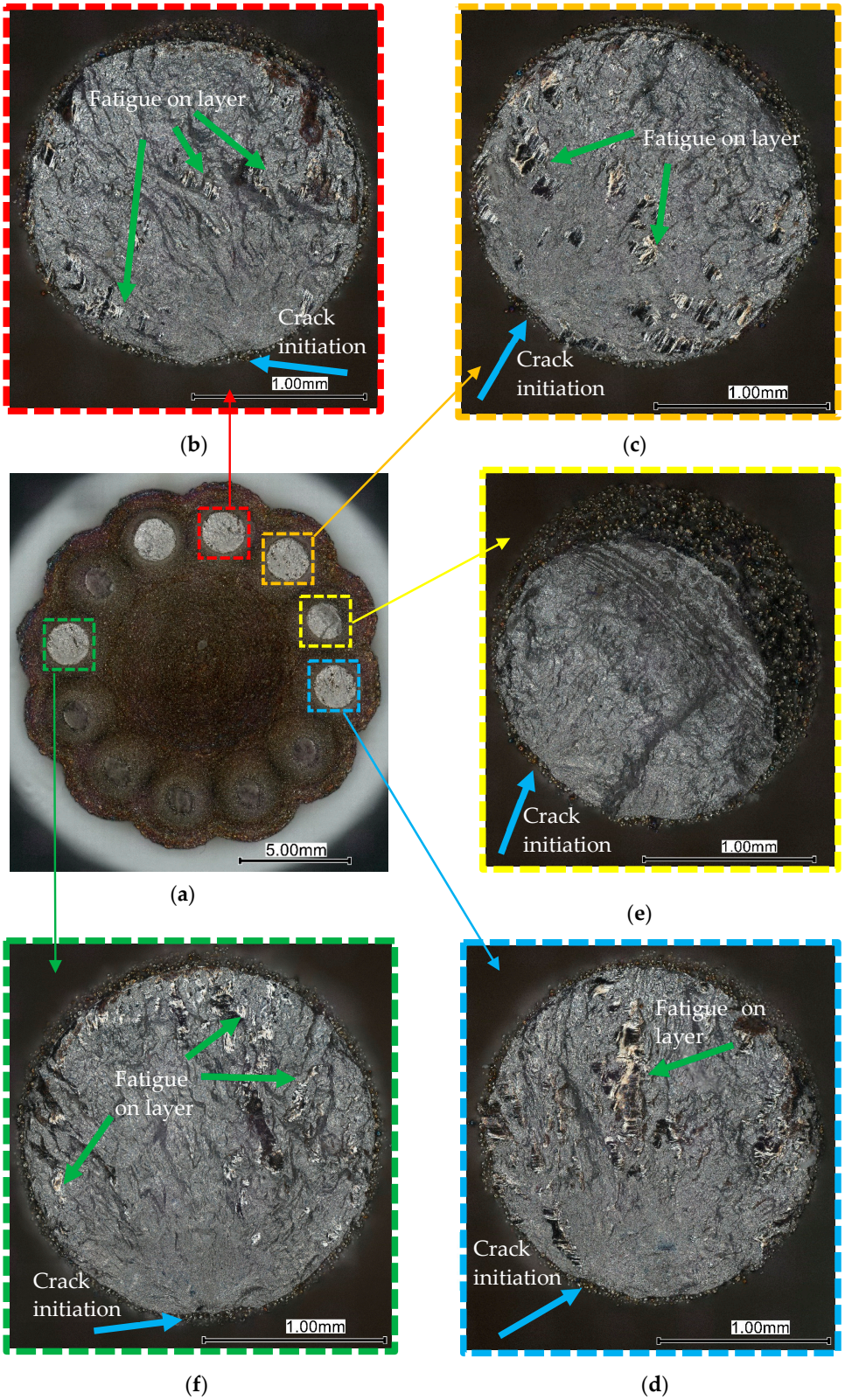

Figure 29. Fracture surface of the N12 geometry tested at a maximum stress level of 280 MPa: (**a**) fracture surface after the fatigue test, (**b**) crack growth surface, (**c**) crack growth surface, (**d**) crack growth surface, (**e**) crack growth and failure surface, (**f**) crack growth surface. The blue arrow in (**a**) shows the broken rod in (**d**), while the orange arrow in (**a**) shows the detail in (**c**), the yellow arrow in (**a**) shows the detail in (**e**). The green arrows in (**d**,**f**) show fatigue at the ply, where the blue arrow shows the initiation of a crack on the bar surface.

4. Discussion

Comparison of surface roughness values between the two geometries used for fatigue testing revealed that they were similar in the middle part of the specimen, where the geometry was constant and devoid of overhangs. Overhangs typically increase surface roughness due to the thermal dynamics inherent in additive manufacturing processes. Maintaining stable and comparable surface roughness is critical when comparing the fatigue behaviors of different geometries, as surface roughness influences fatigue near the surface significantly. However, the impact of internal and subsurface defects, identified through the Archimedes method, also plays a crucial role. Notably, the N12 specimen exhibited a density approximately 0.3% higher than that of the N4 specimen, suggesting a greater prevalence of internal and near-surface defects. It is important to note that this density estimation, and, consequently, the inferred quantity of internal defects, considers the entire specimen, not just the tested geometry in the middle part. Therefore, the results from the Archimedes method may be influenced by the overall surface-to-volume ratio of each specimen.

The microstructure analysis provided a detailed examination of material deposition, highlighting internal defects within the rods, as well as near-surface defects. A significant difference was observed in the outer layer near the surface compared to the inner layers. This variation was expected, given that lower energy inputs were used for the outer layers. Consistent with the lower energy input in these near-surface layers, more defects were visible. The largest near-surface defects, which often served as the initiation sites for cracks, were observed to be of comparable size in both the N4 and N12 specimens. These observations suggest that the size of these near-surface defects may be influenced more by the energy input parameters during manufacturing than by the geometries of the specimens themselves.

The variation in material properties was evaluated by measurement of the Vickers hardness. High variations in the measured values in both directions of measurement can be explained due to the complex thermal history of the material, due to which it cannot be expected for Vickers hardness to be the same across the entire measured surface. Furthermore, the measurements were performed in different areas of melted pool material; therefore, differences were expected. Only the N12 measurements of Vickers hardness in a parallel direction relative to the build plate showed continuity, with values increasing from the outer to the inner part of the specimen. However, the measured values are still comparable with the deviations of other measurements.

The variation in material properties were evaluated using Vickers hardness measurements, which exhibited significant variations across both measurement directions. This variability can be attributed largely to the complex thermal history of the material, which inherently produces differences in hardness throughout the manufactured specimen. Given that the Vickers hardness HV is not expected to remain consistent across the entire measured surface, these findings align with the intrinsic properties of additive manufacturing. Additionally, variations in hardness were anticipated, as the measurements were conducted on various sections of the melted pool material. Notably, the N12 measurements of Vickers hardness in the direction parallel to the build plate displayed consistency, with values increasing gradually from the outer to the inner part of the specimen. Despite this trend, the measured values still showed comparable deviations when contrasted with measurements from other directions, underscoring the heterogeneous nature of the material properties due to its variable thermal history.

Fatigue testing showed that the number of cycles to failure was similar between both specimen geometries at higher stress values, although notable differences emerged at lower stress values. At lower stress levels, the N4 specimens withstood more cycles at the same stress level consistently compared to the N12 specimens, as the N12 specimens had more rods and therefore more possible locations along the outer surfaces where a fatigue crack could initiate compared to an N4 specimen.

Differences in how cracks initiate and propagate under varying stress levels between these two geometries highlight the complex interplay between internal defects, material properties, and geometric factors in determining cycles to failure. It is important to highlight that, at the same stress level of maximum stress, 300 MPa, and the same loading ratio of $R = 0.1$, the number of cycles to failure increased up to three times for N4 compared to N12.

The second key factor is crack initiation. In standardized fatigue tests, crack initiation typically occurs once; however, in the tested geometries of this study, multiple initiations were necessary before the specimens failed. This was evident, as multiple rods in all specimens displayed surfaces where fatigue cracks had propagated. Notably, all the initial cracks originated on the outer surface, specifically at locations marked by visible geometric defects or pores. Comparing the positions of these first crack initiation sites with the maximum stress levels determined by FEA indicated that crack initiation does not always coincide with the areas of highest stress predicted by the FEA. For instance, most of the initial crack initiations in both tested geometries occurred on the part of the rod in the middle part of the specimen. This observation aligns with the FEA-predicted maximum stress location for the N12 specimen but contrasts with the FEA results for the N4 specimen, which suggested that the maximum stress should occur on the opposite side of the rod, facing outward. These discrepancies imply that geometric anomalies and other defects are crucial in determining crack initiation sites, suggesting a higher concentration of defects in the areas of the rods facing the center of the specimen. This increased defect density could be attributed to variations in the manufacturing process, arising from differential thermal conditions in that specific area. This hypothesis is supported by the pattern of subsequent crack initiations, which occurred in the same areas of specimen as the first cracks. Furthermore, the extent of crack propagation varied with the stress level applied during testing. At lower stress levels, only one of the remaining rods exhibited partial fatigue crack propagation. In contrast, specimens tested at higher stress levels displayed multiple rods with partial fatigue crack propagation. This suggests that, at higher stress levels, cracks initiate at multiple sites simultaneously, allowing for concurrent propagation of multiple cracks.

The fracture surfaces of the specimens exhibited intriguing behaviors, characterized by brighter areas that align with the direction of laser travel during the manufacturing process. These areas are observed in sections of the specimens subjected to lower stress levels during fatigue crack growth. Notably, such markings are absent in areas that underwent LCF or experienced significant plastic deformation. This pattern suggests that the path of fatigue crack growth is influenced by stress intensity. Specifically, at lower stress levels, cracks are able to propagate along the boundaries between the melted pools, following the inherent lines of weakness, despite requiring minor deviations in direction. This behavior underscores the impact of the additive manufacturing process on material integrity, where the layer-by-layer construction creates natural fault lines that can dictate crack propagation under certain conditions.

5. Conclusions

The effects of the free surface on the dynamic tensile strength of AISI 316L steel were investigated using two types of specimens made at the same time with the same energy input through selective laser melting (SLM). The concept of this study was based on using detailed numerical modeling and simulation to obtain same stress conditions in the cross sections of specimens with 4 and 12 bars. However, the following conclusions can be drawn from the results of this study:

- Different ratios of area and circumference have an impact on the results of fatigue life of the tested AISI 316L stainless-steel structure specimens manufactured with additive manufacturing, as the fatigue lives of the different structure specimen geometries were different at the same stress level. Therefore, it is necessary to consider circumference as a parameter of fatigue life in such structures.

- Fractography revealed that crack initiations occurred on the outer surfaces due to surface and near-surface defects, indicating that the outer layer of the material is crucial for the fatigue behavior of additive manufactured AISI 316L stainless steel due to bending moments which cannot be avoided fully.
- The direction of fatigue crack propagation is dependent on the stress level, as, at lower levels, the crack deviates to the boundary between the melted pools during manufacturing.
- Simultaneous multiple crack initiation locations are more likely to occur at higher stress levels, as the stress intensity factor around defects reaches higher values that can allow faster crack initiation.
- Smaller differences in the achieved number of cycles between the specimens with 4 and 12 bars are at a higher stress level of loading, while at lower stress levels, the number of achieved cycles in the specimen with 4 bars was more than three times greater.

This study represents a starting point for designers and constructors, indicating that when planning the service life of structural components, in addition to the strength of the material, they must also consider the extent of the free surface, both for the height of the loading stress and for achieving the design-prescribed number of loading cycles. The article explains the reasons why a specimen with a larger circumference-to-cross-section-area ratio will break earlier at the same stress level of loading than a specimen with a smaller circumference-to-cross-section-area ratio.

This finding is important for setting a strategy for printing components with additive manufacturing technologies. By reducing the ratio between the circumference-to-cross-section-area in the critical part of a component, it is possible to ensure a longer service life of a structural component which is manufactured using additive technologies from the same material.

Author Contributions: Conceptualization, N.G.; methodology, L.F. and M.Š.; software, L.F. and F.J. (development and analysis); investigation, F.J. (experimental investigation), M.Š., I.D. (experimental investigation) and N.G.; writing—original draft, L.F. and F.J.; supervision, I.D. and N.G.; project administration, N.G.; funding acquisition, M.Š. and N.G. All authors have read and agreed to the published version of the manuscript.

Funding: Slovenian Agency for Research and Development ARIS for funding Research Program P2-0137 "Numerical and Experimental Analysis Mechanical Systems" and Metal Centre Čakovec in Croatia under the project KK.01.1.1.02.0023.

Data Availability Statement: The raw data supporting the conclusions of this article will be made available by the authors on request.

Acknowledgments: The authors would like to acknowledge the support of the Slovenian Agency for Research and Development ARIS for funding Research Program P2-0137 "Numerical and Experimental Analysis Mechanical Systems" and Metal Centre Čakovec in Croatia under the project KK.01.1.1.02.0023.

Conflicts of Interest: The authors declare no conflict of interest.

References

1. Chen, H.; Gu, D.; Dai, D.; Ma, C.; Xia, M. Microstructure and composition homogeneity, tensile property, and underlying thermal physical mechanism of selective laser melting tool steel parts. *Mater. Sci. Eng. A* **2017**, *682*, 279–289. [CrossRef]
2. Khorasani, M.; Ghasemi, A.; Rolfe, B.; Gibson, I. Additive manufacturing a powerful tool for the aerospace industry. *Rapid Prototyp. J.* **2022**, *28*, 87–100. (In English) [CrossRef]
3. Liu, R.; Wang, Z.; Sparks, T.; Liou, F.; Newkirk, J. Aerospace applications of laser additive manufacturing. In *Laser Additive Manufacturing*; Brandt, M., Ed.; Woodhead Publishing: Cambridge, UK, 2017; pp. 351–371.
4. Leal, R.; Barreiros, F.M.; Alves, L.; Romeiro, F.; Vasco, J.C.; Santos, M.; Marto, C. Additive manufacturing tooling for the automotive industry. *Int. J. Adv. Manuf. Technol.* **2017**, *92*, 1671–1676. [CrossRef]
5. Dwivedi, G.; Srivastava, S.K.; Srivastava, R.K. Analysis of Barriers to Implement Additive Manufacturing Technology in the Indian Automotive Sector. *Int. J. Phys. Distrib. Logist. Manag.* **2017**, *47*, 972–991. [CrossRef]

6. Salifu, S.; Desai, D.; Ogunbiyi, O.; Mwale, K. Recent development in the additive manufacturing of polymer-based com-posites for automotive structures—A review. *Int. J. Adv. Manuf. Technol.* **2022**, *119*, 6877–6891. [CrossRef]
7. Böckin, D.; Tillman, A.-M. Environmental assessment of additive manufacturing in the automotive industry. *J. Clean. Prod.* **2019**, *226*, 977–987. [CrossRef]
8. Stern, F.; Kleinhorst, J.; Tenkamp, J.; Walther, F. Investigation of the anisotropic cyclic damage behavior of selective laser melted AISI 316L stainless steel. *Fatigue Fract. Eng. Mater. Struct.* **2019**, *42*, 2422–2430. [CrossRef]
9. Vignesh, M.; Ranjith Kumar, G.; Sathishkumar, M.; Manikandan, M.; Rajyalakshmi, G.; Ramanujam, R.; Arivazhagan, N. Development of Biomedical Implants through Additive Manufacturing: A Review. *J. Mater. Eng. Perform.* **2021**, *30*, 4735–4744. [CrossRef]
10. Oliveira, T.T.; Reis, A.C. Fabrication of dental implants by the additive manufacturing method: A systematic review. *J. Prosthet. Dent.* **2019**, *122*, 270–274. [CrossRef]
11. Mohammed, M.; Gibson, I. Applications of 3D topography scanning and multi-material additive manufacturing for facial prosthesis development and production. In Proceedings of the 27th Annual International Solid Freeform Fabrication Symposium-An Additive Manufacturing Conference, SFF 2016, Austin, TX, USA, 8–10 August 2016.
12. Soares, B.; Ribeiro, I.; Cardeal, G.; Leite, M.; Carvalho, H.; Peças, P. Social life cycle performance of additive manufacturing in the healthcare industry: The orthosis and prosthesis cases. *Int. J. Comput. Integr. Manuf.* **2021**, *34*, 327–340. [CrossRef]
13. Roland, T.; Retraint, D.; Lu, K.; Lu, J. Fatigue life improvement through surface nanostructuring of stainless steel by means of surface mechanical attrition treatment. *Scr. Mater.* **2006**, *54*, 1949–1954. [CrossRef]
14. Avanzini, A. Fatigue Behavior of Additively Manufactured Stainless Steel 316L. *Materials* **2022**, *16*, 65. [CrossRef]
15. D'andrea, D. Additive Manufacturing of AISI 316L Stainless Steel: A Review. *Metals* **2023**, *13*, 1370. [CrossRef]
16. Shamsujjoha; Agnew, S.R.; Fitz-Gerald, J.M.; Moore, W.R.; Newman, T.A. High Strength and Ductility of Additively Manufactured 316L Stainless Steel Explained. *Met. Mater. Trans. A* **2018**, *49*, 3011–3027. [CrossRef]
17. Javidrad, H.; Koc, B.; Bayraktar, H.; Simsek, U.; Gunaydin, K. Fatigue performance of metal additive manufacturing: A comprehensive overview. *Virtual Phys. Prototyp.* **2024**, *19*, 2302556. [CrossRef]
18. Akgun, E.; Zhang, X.; Biswal, R.; Zhang, Y.; Doré, M. Fatigue of Wire + Arc Additive Manufactured Ti-6Al-4V in Presence of Process-Induced Porosity Defects. *Int. J. Fatigue* **2021**, *150*, 106315. [CrossRef]
19. Leuders, S.; Thöne, M.; Riemer, A.; Niendorf, T.; Tröster, T.; Richard, H.; Maier, H. On the mechanical behaviour of titanium alloy TiAl6V4 manufactured by selective laser melting: Fatigue resistance and crack growth performance. *Int. J. Fatigue* **2012**, *48*, 300–307. [CrossRef]
20. Edwards, P.; Ramulu, M. Fatigue performance evaluation of selective laser melted Ti–6Al–4V. *Mater. Sci. Eng. A* **2014**, *598*, 327–337. [CrossRef]
21. Zerbst, U.; Madia, M.; Bruno, G.; Hilgenberg, K. Towards a Methodology for Component Design of Metallic AM Parts Subjected to Cyclic Loading. *Metals* **2021**, *11*, 709. [CrossRef]
22. Morgan, R.; Sutcliffe, C.J.; O'Neill, W. Density analysis of direct metal laser re-melted 316L stainless steel cubic primitives. *J. Mater. Sci.* **2004**, *39*, 1195–1205. [CrossRef]
23. King, W.E.; Barth, H.D.; Castillo, V.M.; Gallegos, G.F.; Gibbs, J.W.; Hahn, D.E.; Kamath, C.; Rubenchik, A.M. Observation of keyhole-mode laser melting in laser powder-bed fusion additive manufacturing. *J. Mater. Process. Technol.* **2014**, *214*, 2915–2925. [CrossRef]
24. Svensson, M.; Thundal, M. Titanium alloys manufactured with Electron Beam Melting—Mechanical and Chemical properties. In Proceedings of the Materials and Processes for Medical Devices Conference, Minneapolis, MN, USA, 10–12 August 2009.
25. Darvish, K.; Chen, Z.; Pasang, T. Reducing lack of fusion during selective laser melting of CoCrMo alloy: Effect of laser power on geometrical features of tracks. *Mater. Des.* **2016**, *112*, 357–366. [CrossRef]
26. Mukherjee, T.; Zuback, J.S.; De, A.; DebRoy, T. Printability of alloys for additive manufacturing. *Sci. Rep.* **2016**, *6*, 19717. [CrossRef]
27. Fatemi, A.; Molaei, R.; Simsiriwong, J.; Sanaei, N.; Pegues, J.; Torries, B.; Phan, N.; Shamsaei, N. Fatigue behaviour of additive manufactured materials: An overview of some recent experimental studies on Ti-6Al-4V considering various processing and loading direction effects. *Fatigue Fract. Eng. Mater. Struct.* **2019**, *42*, 991–1009. [CrossRef]
28. Sanaei, N.; Fatemi, A.; Phan, N. Defect characteristics and analysis of their variability in metal L-PBF additive manufacturing. *Mater. Des.* **2019**, *182*, 108091. [CrossRef]
29. Sanaei, N.; Fatemi, A. Analysis of the Effect of Surface Roughness on Fatigue Performance of Powder Bed Fusion Additive Manufactured Metals. *Theor. Appl. Fract. Mech.* **2020**, *108*, 102638. [CrossRef]
30. Zhang, B.; Li, Y.; Bai, Q. Defect Formation Mechanisms in Selective Laser Melting: A Review. *Chin. J. Mech. Eng.* **2017**, *30*, 515–527. [CrossRef]
31. Gu, D.; Shen, Y. Balling phenomena in direct laser sintering of stainless steel powder: Metallurgical mechanisms and control methods. *Mater. Des.* **2009**, *30*, 2903–2910. [CrossRef]
32. Rahmati, S.; Vahabli, E. Evaluation of analytical modeling for improvement of surface roughness of FDM test part using measurement results. *Int. J. Adv. Manuf. Technol.* **2015**, *79*, 823–829. [CrossRef]
33. du Plessis, A.; Beretta, S. Killer notches: The effect of as-built surface roughness on fatigue failure in AlSi10Mg produced by laser powder bed fusion. *Addit. Manuf.* **2020**, *35*, 101424. [CrossRef]

34. Greitemeier, D.; Donne, C.D.; Syassen, F.; Eufinger, J.; Melz, T. Effect of surface roughness on fatigue performance of additive manufactured Ti–6Al–4V. *Mater. Sci. Technol.* **2015**, *32*, 629–634. [CrossRef]
35. Spierings, A.; Starr, T.; Wegener, K. Fatigue performance of additive manufactured metallic parts. *Rapid Prototyp. J.* **2013**, *19*, 88–94. [CrossRef]
36. Afkhami, S.; Dabiri, M.; Piili, H.; Björk, T. Effects of manufacturing parameters and mechanical post-processing on stainless steel 316L processed by laser powder bed fusion. *Mater. Sci. Eng. A* **2020**, *802*, 140660. [CrossRef]
37. Slotwinski, J.A.; Garboczi, E.J.; Hebenstreit, K.M. Porosity Measurements and Analysis for Metal Additive Manufacturing Process Control. *J. Res. Natl. Inst. Stand. Technol.* **2014**, *119*, 494–528. [CrossRef]
38. Murakami, Y. Effects of Small Defects and Nonmetallic Inclusions on the Fatigue Strength of Metals. *JSME Int. J. Ser. 1 Solid Mech. Strength Mater.* **1989**, *32*, 167–180. [CrossRef]
39. EOS GmbH. Eos M 290. Available online: https://www.eos.info/en-us/metal-solutions/metal-printers/eos-m-290#key-features (accessed on 10 June 2024).
40. *ISO 15350:2000*; Steel and Iron—Determination of Total Carbon and Sulfur Content—Infrared Absorption Method After Combustion in an Induction Furnace. International Organization for Standardization: Geneva, Switzerland, 15 December 2000.
41. M4P 316L Datasheet, M4P, Krefeld, Germany. Available online: https://www.metals4printing.com/wp-content/uploads/datasheets/de/Fe-Basis/m4p_Datenblatt_316L_DE.pdf (accessed on 12 June 2024).
42. *ISO 6892-1:2019*; Metallic Materials—Tensile Testing—Part 1: Method of Test at Room Temperature. International Organization for Standardization: Geneva, Switzerland, 3 January 2020.
43. Jagarinec, D.; Gubeljak, N. Effect of Residual Stresses on the Fatigue Stress Range of a Pre-Deformed Stainless Steel AISI 316L Exposed to Combined Loading. *Metals* **2024**, *14*, 1084. [CrossRef]
44. *ISO 21920-3:2021*; Geometrical Product Specifications (GPS)—Surface Texture: Profile—Part 3: Specification Operators. International Organization for Standardization: Geneva, Switzerland, 20 December 2021.
45. Hatami, S.; Ma, T.; Vuoristo, T.; Bertilsson, J.; Lyckfeldt, O. Fatigue Strength of 316 L Stainless Steel Manufactured by Selective Laser Melting. *J. Mater. Eng. Perform.* **2020**, *29*, 3183–3194. [CrossRef]